Contrib Mineral Petrol (2012) 164:407–426
DOI 10.1007/s00410-012-0744-6

ORIGINAL PAPER

# Peralkaline magma evolution and the tephra record in the Ethiopian Rift

**Tyrone O. Rooney · William K. Hart · Chris M. Hall · Dereje Ayalew · Mark S. Ghiorso · Paulo Hidalgo · Gezahegn Yirgu**

Received: 7 November 2011 / Accepted: 26 March 2012 / Published online: 19 April 2012


**Abstract** The 3.119 ± 0.010 Ma Chefe Donsa phreatomagmatic deposits on the shoulder of the Ethiopian Rift mark the northern termination of the Silti-Debre Zeyit Fault Zone, a linear zone of focused extension within the modern Ethiopian Rift. These peralkaline pumice fragments and glass shards span a wide range of glass compositions but have a restricted phenocryst assemblage dominated by unzoned sanidine. Glass shards found within the ash occupy a far more limited compositional range (75–76 wt% $SiO_2$) in comparison with the pumice (64–75 wt% $SiO_2$), which is rarely mingled. Thermodynamic modeling shows that liquids broadly similar to the least evolved glass composition can be achieved with 50–60 % fractionation of moderately crustally contaminated basalt. Inconsistencies between modeled solutions and the observed values of CaO and $P_2O_5$ highlight the important role of fluorine in stabilizing fluor-apatite and the limitations of current thermodynamic models largely resulting from the scarce experimental data available for the role of fluorine in igneous phase stability. On the basis of limited feldspar heterogeneity and crystal content of pumice at Chefe Donsa, and the difficulties of extracting small volumes of Si-rich melt in classical fractional crystallization models, we suggest a two-step polybaric process: (1) basaltic magma ponds at mid-upper-crustal depths and fractionates to form a crystal/magma mush. Once this mush has reached 50–60 % crystallinity, the interstitial liquid may be extracted from the rigid crystal framework. The trachytic magma extracted at this step is equivalent to the most primitive pumice analyzed at Chefe Donsa. (2) The extracted trachytic liquid will rise and continue to crystallize, generating a second mush zone from which rhyolite liquids may be extracted. Some of the compositional range observed in the Chefe Donsa deposits may result from the fresh intrusion of trachyte magma, which may also provide an eruption trigger. This model may have wider application in understanding the origin of the Daly Gap in Ethiopian magmas—intermediate liquids may not be extracted from crystal-liquid mushes due to insufficient crystallization to yield a rigid framework. The wide range of glass compositions characteristic of the proximal Chefe Donsa deposits is not recorded in temporally equivalent tephra deposits located in regional depocenters. Our results show that glass shards, which represent the material most likely transported to distal depocenters, occupy a limited compositional range at high $SiO_2$ values and overlap some distal tephra deposits. These results suggest that distal tephra deposits may not faithfully record the potentially

Communicated by T. L. Grove.

**Electronic supplementary material** The online version of this article (doi:10.1007/s00410-012-0744-6) contains supplementary material, which is available to authorized users.

T. O. Rooney (✉) · P. Hidalgo
Department of Geological Sciences, Michigan State University, East Lansing, MI 48824, USA
e-mail: rooneyt@msu.edu

W. K. Hart
Department of Geology & Environmental Earth Science, Miami University, Oxford, OH 45056, USA

C. M. Hall
Department of Earth and Environmental Sciences, University of Michigan, Ann Arbor, MI 48109, USA

D. Ayalew · G. Yirgu
Department of Earth Sciences, Addis Ababa University, P.O. Box 1176, Addis Ababa, Ethiopia

M. S. Ghiorso
OFM Research, 7336 24th Ave NE, Seattle, WA 98115, USA

wide range in magma compositions present in a magmatic system just prior to eruption and that robust distal–proximal tephra correlations must include a careful analysis of the full range of materials in the proximal deposit.

**Keywords** East African Rift · Ethiopia · Peralkaline · Tephra · MELTS

## Introduction

The magmatic sequences of the East African rift system have long been recognized as important probes of the tectonic processes active within this type location of continental rifting. In addition, proximal and distal tephra horizons, which are intercalated within hominid-bearing sedimentary deposits, provide the potential for significant temporal control through the use of radiogenic isotopes and chemical correlation of the tephra. Large-scale phreatomagmatic eruptions produce deposits of chemically distinctive pumice, glass, and crystals that can be distributed and preserved over a wide spatial area, and therefore act as temporal marker horizons. It is the apparent distinction in the composition of these magmatic components that allows for correlation between stratigraphic sections; however, such correlations require assumptions such as the homogeneity of erupted material and the uniqueness of a particular glass or crystal composition to one eruptive episode. Advances in the understanding of the origin of large-volume silicic magmas (e.g., Bachmann and Bergantz 2004, 2008; Deering et al. 2011b) have questioned the validity of such assumptions and necessitate a renewed focus on magmatic processes during individual eruptive episodes. In particular, peralkaline magmatic systems, which are commonly found in continental rift settings, present a challenge for tephra geochemical fingerprinting as geochemical zoning of magmas chambers is pervasive (e.g., MacDonald and Scaillet 2006).

Typically, silicic activity in the Ethiopian Rift and Afar is focused on large silicic centers, built up over multiple eruptive episodes, later dissected by faulting and basaltic activity (Lahitte et al. 2003; Peccerillo et al. 2003). The Chefe Donsa edifice presents an unusual opportunity in the Ethiopian Rift to explore what is likely a single episode of explosive silicic volcanism and to probe the magma chamber processes that led to the formation of this deposit. In this contribution, we present pumice, glass, and crystal compositions for a proximal phreatomagmatic deposit on the margin of the Main Ethiopian Rift. In addition, we present high-resolution $^{40}Ar/^{39}Ar$ data from single sanidine crystals. Here, we show that the wide range in glass compositions found in proximal peralkaline deposits may not be preserved in distal depocenters, and we explore the complexities of thermodynamic modeling of F-rich magmas. These data provide a window into processes active in peralkaline magmatic centers throughout the region and may be used to develop our understanding of the origin of silicic magmatism during continental rift development.

## Magmatic and tectonic setting

The East African rift system (EARS), one of the best exposed continental rifts in the world, preserves a rich Cenozoic magmatic record that is dominated by the interaction between mantle plume(s) and extensional tectonics. Initial magmatic activity (45–31 Ma) occurred dominantly in southern Ethiopia and northern Kenya but was followed by a widespread flood basalt event between ~31 and 29 Ma (Hofmann et al. 1997; George et al. 1998). These flood basalts occupy approximately 600,000 $km^2$ throughout Ethiopia, eastern Sudan, and southern Yemen (Mohr and Zanettin 1988). The development of shield volcanoes on the Ethiopian plateaus and the continued magmatism in northern Kenya dominated the region until the development of more spatially widespread, but temporally asynchronous rift-related volcanism (e.g., Kieffer et al. 2004; Furman et al. 2006; Rooney et al. 2011, 2012).

The Main Ethiopian Rift (MER), which is located at northern end of the EARS, has developed in sectors over the past ~20 Ma. The youngest central sector of the MER (the focus of this study) developed coincident with silicic volcanism along the rift shoulder at ~10–12 Ma (Wolfenden et al. 2004). Subsequently, magmatic activity became largely focused on two magmatic–tectonic features on the rift floor—the Wonji Fault Belt (Mohr 1967; Ebinger and Casey 2001; Rooney et al. 2007) and the Silti-Debre Zeyit Fault Zone (WoldeGabriel et al. 1990; Rooney et al. 2005; Rooney 2010). The Chefe Donsa edifice lies on the Ethiopian Plateau along a northerly extension of the Silti-Debre Zeyit Fault Zone. The modern magmatic expression of the Wonji Fault Belt and Silti-Debre Zeyit Fault Zone is a bimodal association of aligned chains of basaltic cinder cones located between large central silicic volcanoes. The Chefe Donsa edifice is consistent with this magmatic association and is aligned with the silicic centers of Ziqualla and Bede Gebebe, in between which maars, cinder cones, and mafic flows are dominant (Fig. 1). These magmatic–tectonic fault belts are a key feature in the evolution of the rift and are thought to accommodate the majority of modern extension in the region (e.g., Bilham et al. 1999; Ebinger and Casey 2001; Casey et al. 2006), yet the exact process of lithospheric weakening associated with this transition is uncertain. It remains unclear if the ~4 km × 2.2 km Chefe Donsa structure (Fig. 1b) is a tuff ring or caldera; some subsidence of the floor (~2,250–2,270 m) is evident in

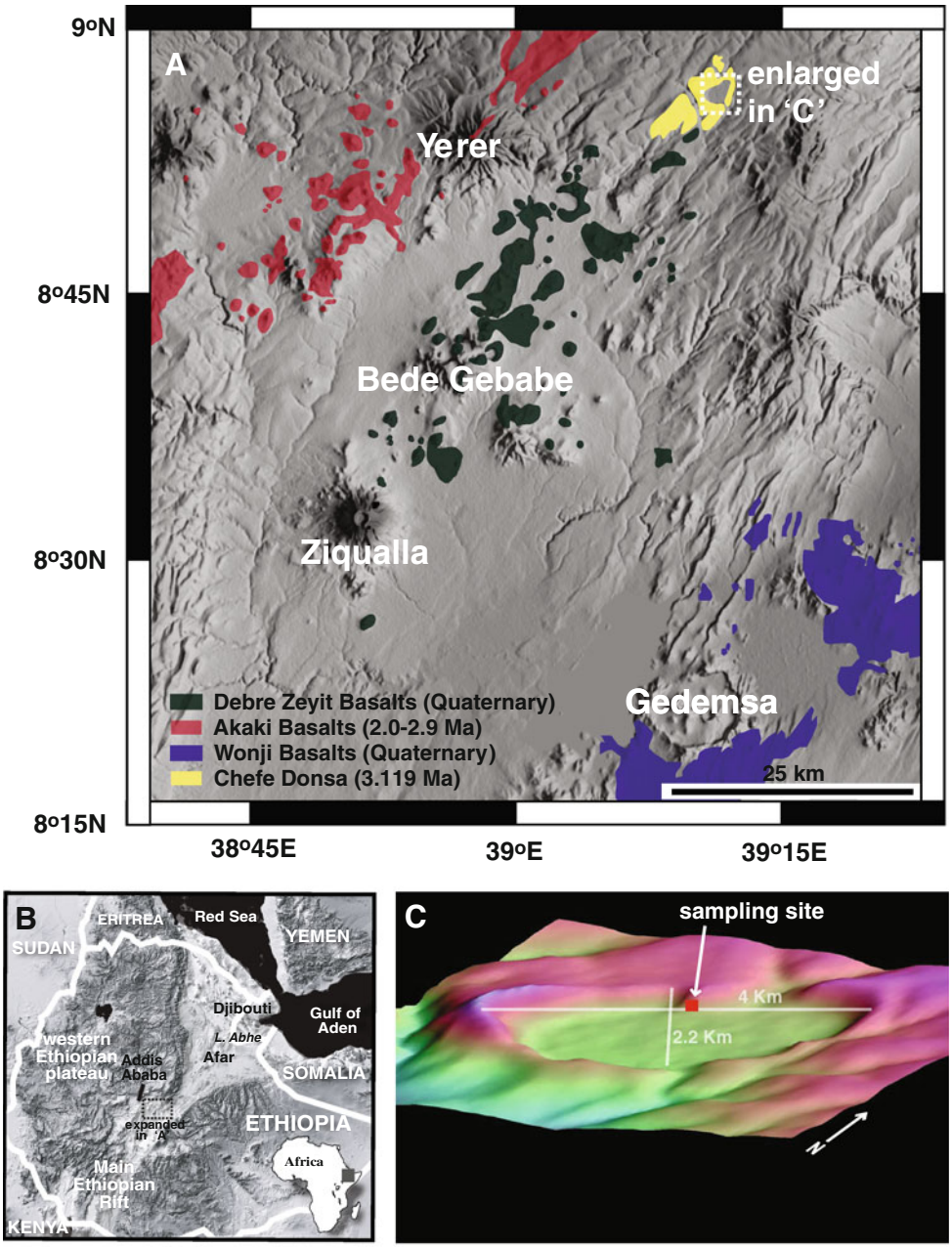


**Fig. 1** **a** Map of the Central portion of the Main Ethiopian Rift study area with fields added for the Wonji, Debre Zeyit, and Akaki basalts. Notable felsic volcanoes and calderas are named in white. The Chefe Donsa phreatomagmatic deposits are highlighted in *yellow*. **b** Regional map showing East Africa and the region that is expanded in 'A'. **c** Closeup reflectance image of the Chefe Donsa edifice with a 4× vertical exaggeration. The two sampling locations are too close to be resolvable and are highlighted as a *single dot*. Backgrounds are reflectance images of East Africa and Yemen from the NASA/JPL Shuttle Radar Tomography Mission (USGS 2004)

comparison with the surrounding northern portion of the edifice (~2,300–2,350 m), though a broad decrease in topography to the south is also apparent. In this paper, we refer to the edifice as a caldera, recognizing that the final designation awaits further study.

## Methods and results

### Petrography

Field investigation and petrographic analysis of thin sections reveal that the deposit consists of pumice, glass shards, and sanidine set in an ashy matrix. Lithic fragments are present and are weathered. Some possible older pumice fragments were identified (yellowish and tan colors) and are typically more altered, with some devitrification. On thin section scale, most juvenile pumice are aphyric, though up to ~20 % crystal content (feldspar) can be observed. Three varieties of pumice were identified: felsic (clear), mafic (brownish to dark), and mixed. Only one type of shard population has been identified with shards typically semi-flat in shape, indicating some degree of welding. Sanidine crystals are pervasive in the sections and are found within the pumice and ash. These sanidine crystals are frequently fractured, with some broken. Resorption of

the sanidine crystals is also observed but is non-systematic (extending throughout the crystal). Quartz crystals are less abundant and are also typically fractured and broken. Less frequently observed are crystals of aenigmatite, Fe-Ti oxides, and aegirine-augite.

## Whole-rock data and glass

Two bulk samples of pumice, ash, and scoria were taken from the wall of the Chefe Donsa caldera. These samples were disaggregated, and individual pumice clasts (3–20 cm) were extracted and cleaned in an ultrasonic bath with deionized water to remove adhering ash. Results are presented in Tables 1 and 2; full sample preparation, analytical methods, and results are available in the online supplementary material. XRF-determined whole-rock pumice clast compositions show a slightly wider range in $SiO_2$ (64–75 % $SiO_2$) in comparison with electron microprobe (EMP)-determined glass compositions within pumice fragments (68–75 % $SiO_2$); however, the glass shards analyzed from within the ash are much more restricted in composition (75–76 % $SiO_2$; all normalized to 100 %). The major element characteristics of pumice clasts, pumice glass, and glass shards from Chefe Donsa define a wide array of compositions extending from comenditic trachyte and trachydacite to rhyolite (see online supplementary materials). CIPW norm values, calculated using the software IUGSTAS (Le Maitre 2002), reveal that $q + an$ assemblages are typical for the trachytes and tracydacites (metalumnous/mildly peralkaline), while $q + ac$ assemblages characterize the rhyolites (uniformly peralkaline).

Establishing the differentiation trends within peralkaline magmas is complicated by fractional crystallization, which has the potential to decrease the $SiO_2$ content of peralkaline residual liquids (Scaillet and MacDonald 2001). In such cases, the peralkalinity index (PI) more robustly assesses the degree of magma evolution (e.g., Marshall et al. 2009); however, at Chefe Donsa, the strong positive correlation between PI and $SiO_2$ (Fig. 2) suggests that $SiO_2$ remains an appropriate choice. Multiple analyses of glass compositions within pumice fragments typically revealed little variability, though some scatter in $Na_2O$, $K_2O$, and $Fe_2O_3$ is observed (Fig. 2). Two pumice fragments that were petrographically categorized as 'mingled' display a significant range in $SiO_2$ compositions (69–72 wt% and 71–74 wt%), which is consistent with some pre-eruptive magma heterogeneity in the Chefe Donsa system. Major element variation with $SiO_2$ shows a continuous decrease in $TiO_2$, $Al_2O_3$, CaO, $P_2O_5$, while FeO* remains somewhat constant. $K_2O$ and $Na_2O$ appear to have conjugate patterns: $K_2O$ increases in concentration, peaking at 69 % $SiO_2$, and drops thereafter; $Na_2O$ concentrations decrease until ~69 % $SiO_2$ and remain constant thereafter. These major element trends broadly mirror those in the nearby silicic center of Bede Gebebe, though Chefe Donsa extends to more elevated values of $TiO_2$ (Fig. 2).

Trace elements in the Chefe Donsa pumice typically show a hyperbolic enrichment (e.g., La, Y, Nb) or depletion (Ba) on Harker diagrams as the magma composition passes from trachyte to rhyolite (Fig. 3). Notable exceptions are the positive linear arrays formed by Zr and Rb, and the U-shaped trend formed by Eu, reaching a minimum concentration at ~69 % $SiO_2$. Trace elements trends at Chefe Donsa mirror values at Bede Gebebe, Yerer, and Ziqualla; however, Zr and Rb are distinctly lower at Chefe Donsa (Fig. 3). Chondrite-normalized REE diagrams (Fig. 4) illustrate that rhyolites are displaced toward higher REE concentrations and display more significant Eu anomalies in comparison with the trachytes (though the absolute concentration of Eu is either equivalent to or greater than that of the trachytes). These major and trace element data (e.g., U-shaped Eu variation diagrams, linear Rb enrichment, conjugate increases and decreases in $Na_2O$ and $K_2O$ concentrations) are consistent with existing models from other peralkaline centers where the majority of geochemical variation can be explained by a shift in feldspar compositions from dominantly Ab to Or as a magma changes toward peralkaline composition (e.g., Scaillet and MacDonald 2001).

## Crystal compositions

Feldspar analyzed from the Chefe Donsa deposit exhibits a limited compositional range ($Or_{37–46}$) with very low Ca (An < 3), and plotting within the sanidine field (Fig. 5). Fe contents are low (FeO* < 1 %), with slightly higher concentrations in higher Or crystals. An embayed crystal did not exhibit compositional heterogeneity ($Or_{40}$) beyond that of the more euhedral feldspar population. Core compositions varied by ~15 % from $Or_{39}$ to $Or_{46}$. Zoning is not apparent in the majority of the crystals examined (less than 1 % Or variation between core and rim); however, one crystal exhibits some minor variability from a $Or_{40}$ core to a $Or_{37}$ rim. In comparison with other regional suites, Chefe Donsa feldspars plot in a similar field to other peralkaline magmas, occupying some of the most Or-rich compositions for feldspars in Ethiopia (Fig. 5).

## Ar Geochronology

Sanidine crystals hosted within a larger pumice clast were handpicked from sample 2012A and prepared following the method outlined in the online supplementary material. The

**Table 1** Whole-rock XRF and ICP-MS analyses for samples in this study

| Samples | $SiO_2$ (%) | $TiO_2$ (%) | $Al_2O_3$ (%) | $Fe_2O_3$ (%) | MnO (%) | MgO (%) | CaO (%) | $Na_2O$ (%) | $K_2O$ (%) | $P_2O_5$ (%) | Totals |
|---|---|---|---|---|---|---|---|---|---|---|---|
| 2012B | 62.43 | 0.74 | 14.94 | 4.98 | 0.85 | 0.51 | 0.99 | 5.34 | 5.45 | 0.16 | 96.39 |
| 2012A | 62.53 | 1.08 | 14.15 | 6.12 | 0.27 | 0.91 | 1.74 | 4.88 | 4.94 | 0.31 | 96.93 |
| 2012B-2 | 69.11 | 0.34 | 10.79 | 4.48 | 0.21 | 0.13 | 0.36 | 4.16 | 4.9 | 0.03 | 94.51 |
| 2012A-3 | 63.4 | 0.69 | 15.15 | 4.86 | 0.29 | 0.38 | 1.04 | 5.35 | 5.6 | 0.13 | 96.89 |
| 2012A-2a | 61.73 | 0.74 | 14.77 | 4.98 | 0.99 | 0.44 | 1.15 | 5.39 | 5.48 | 0.17 | 95.84 |
| 2012B-1 | 62.59 | 0.78 | 15 | 5.18 | 0.75 | 0.45 | 1.15 | 5.33 | 5.47 | 0.17 | 96.87 |
| 2012B-3 | 72.15 | 0.32 | 10.17 | 4.73 | 0.17 | 0 | 0.1 | 3.76 | 5.13 | 0.04 | 96.57 |
| 2012A-5 | 65.72 | 0.54 | 13.64 | 5.25 | 0.24 | 0.2 | 0.57 | 3.76 | 5.96 | 0.1 | 95.98 |
| 2012A-4 | 65.31 | 0.73 | 13.74 | 5.74 | 0.21 | 0.36 | 0.83 | 3.83 | 5.6 | 0.18 | 96.53 |
| 2012A-2b | 71.72 | 0.31 | 10.85 | 4.51 | 0.16 | 0.06 | 0.12 | 3.76 | 5.06 | 0.05 | 96.6 |

| Samples | Rb | Sr | Zr | Ba | La | Ce | Pr | Nd | Sm | Eu | Gd | Tb | Y |
|---|---|---|---|---|---|---|---|---|---|---|---|---|---|
| 2012B | 44 | 18 | 223 | 790 | 51 | 80 | 12.6 | 54 | 12.0 | 3.28 | 11.4 | 1.94 | 60 |
| 2012A | 54 | 61 | 319 | 582 | 44 | 80 | 11.2 | 46 | 9.9 | 2.71 | 10.0 | 1.58 | 56 |
| 2012B-2 | 103 | 9 | 672 | 74 | 85 | 182 | 21.5 | 81 | 16.5 | 1.51 | 18.5 | 2.89 | 112 |
| 2012A-3 | 49 | 12 | 264 | 271 | 41 | 86 | 11.5 | 46 | 9.7 | 2.73 | 9.6 | 1.51 | 51 |
| 2012A-2a | 44 | 21 | 227 | 902 | 47 | 77 | 12.1 | 49 | 9.9 | 3.53 | 10.7 | 1.70 | 65 |
| 2012B-1 | 44 | 20 | 234 | 786 | 45 | 74 | 12.1 | 50 | 10.6 | 3.4 | 10.7 | 1.79 | 60 |
| 2012B-3 | 112 | 4 | 775 | 43 | 146 | 289 | 35.5 | 133 | 26.9 | 2.27 | 29.9 | 5.21 | 199 |
| 2012A-5 | 72 | 9 | 437 | 60 | 42 | 80 | 10.5 | 41 | 8.3 | 1.07 | 8.5 | 1.44 | 52 |
| 2012A-4 | 68 | 25 | 458 | 137 | 49 | 91 | 12.6 | 48 | 9.9 | 1.54 | 10.1 | 1.79 | 64 |
| 2012A-2b | 108 | 9 | 764 | 77 | 153 | 291 | 37.1 | 140 | 28.1 | 2.55 | 30.8 | 5.32 | 199 |

| Samples | Dy | Ho | Er | Yb | Lu | V | Cr | Nb | Hf | Ta | Pb | Th | U |
|---|---|---|---|---|---|---|---|---|---|---|---|---|---|
| 2012B | 11.4 | 2.57 | 7.29 | 7.43 | 1.14 | 18.62 | 3.82 | 51 | 5.53 | 4.26 | 10.55 | 3.89 | 1.34 |
| 2012A | 10.07 | 2.08 | 5.95 | 6.19 | 0.95 | 51.14 | 3.41 | 61 | 8.38 | 4.05 | 9.61 | 5.92 | 1.39 |
| 2012B-2 | 18.14 | 4.03 | 11.71 | 11.73 | 1.83 | 9.85 | 4.86 | 120 | 20.47 | 7.62 | 27.11 | 15.25 | 3.98 |
| 2012A-3 | 8.93 | 1.89 | 5.32 | 5.28 | 0.8 | 8.91 | 2.44 | 53 | 6.61 | 3.58 | 11.27 | 4.96 | 1.27 |
| 2012A-2a | 10.43 | 2.32 | 6.59 | 6.36 | 1.03 | 15.16 | 1.53 | 43 | 5.62 | 4.23 | 8.61 | 4.11 | 1.19 |
| 2012B-1 | 10.92 | 2.43 | 6.98 | 6.98 | 1.08 | 17.91 | 1.83 | 44 | 5.98 | 4.22 | 8.48 | 4.33 | 1.17 |
| 2012B-3 | 32.27 | 7.02 | 20.78 | 20.73 | 3.28 | 11.19 | 16.03 | 198 | 39.36 | 13.12 | 53.92 | 28.94 | 5.5 |
| 2012A-5 | 8.7 | 1.88 | 5.45 | 5.38 | 0.88 | 4.68 | 6.74 | 54 | 9.39 | 3.56 | 11.83 | 7.07 | 1.27 |
| 2012A-4 | 10.99 | 2.37 | 6.78 | 6.63 | 1.06 | 18.52 | 9.16 | 63 | 11.28 | 4.32 | 13.92 | 8.49 | 1.52 |
| 2012A-2b | 32.29 | 7.03 | 20.87 | 21.09 | 3.39 | 17.42 | 18.99 | 188 | 37.99 | 12.71 | 52.06 | 27.83 | 5.33 |

Analytical details are outlined in the online supplemental materials

two-step heating analyses both yield plateau age segments with plateau ages for two replicates of multiple grains being 3.069 ± 0.029 Ma and 3.100 ± 0.018 Ma, respectively (all errors 1$\sigma$). For the analysis of individual crystals, the 17 individual grains lie on an isochron with an apparent age of 3.121 ± 0.010 Ma and an initial $^{40}Ar/^{36}Ar$ ratio of 294.1 ± 1.3 (see online supplementary material). The fitted initial $^{40}Ar/^{36}Ar$ ratio is within error of the atmospheric value of 295.5, and the MSWD for the isochron of 1.31 is compatible with this group of grains being from a single age population ($p = 0.186$). This is further illustrated in the figure showing a histogram of ages derived from individual grains assuming an initial Ar composition identical to air. The histogram is constructed by adding each grain's Gaussian-distributed age estimate. Each grain contributes an identical area under the curve, but unlike traditional histograms, the precision of the measurement can be taken into account. The plot shows that there is a single narrow peak at an apparent age of 3.119 ± 0.010 Ma and this is our preferred age for this sample (Fig. 6).

**Table 2** Electron microprobe analysis of glass from pumice and shards FeO(t) converted to $Fe_2O_3$(t)

| Spot | Material | $SiO_2$ (%) | $TiO_2$ (%) | $Al_2O_3$ (%) | $Fe_2O_3$ (%) | MnO (%) | MgO (%) | CaO (%) | $Na_2O$ (%) | $K_2O$ (%) | Totals |
|---|---|---|---|---|---|---|---|---|---|---|---|
| 11/1 | Pumice B-1 | 66.20 | 0.58 | 13.06 | 5.09 | 0.36 | 0.16 | 0.70 | 4.14 | 6.53 | 96.81 |
| 12/1 | | 64.92 | 0.51 | 13.03 | 5.29 | 0.30 | 0.17 | 0.77 | 4.46 | 5.96 | 95.39 |
| 13/1 | | 67.88 | 0.56 | 14.05 | 5.30 | 0.30 | 0.20 | 0.66 | 4.01 | 6.46 | 99.42 |
| 14/1 | | 66.86 | 0.55 | 13.33 | 5.08 | 0.28 | 0.25 | 0.78 | 3.83 | 6.55 | 97.52 |
| 16/1 | | 66.24 | 0.53 | 13.79 | 5.61 | 0.35 | 0.26 | 0.82 | 5.23 | 5.44 | 98.28 |
| 17/1 | | 66.15 | 0.57 | 13.72 | 5.16 | 0.31 | 0.17 | 0.72 | 4.46 | 6.67 | 97.93 |
| 18/1 | | 65.97 | 0.61 | 13.67 | 5.36 | 0.27 | 0.23 | 0.73 | 4.63 | 6.20 | 97.67 |
| | Average | 66.32 | 0.56 | 13.52 | 5.27 | 0.31 | 0.21 | 0.74 | 4.39 | 6.26 | 97.57 |
| | SD | 0.90 | 0.03 | 0.39 | 0.19 | 0.03 | 0.04 | 0.05 | 0.46 | 0.43 | 1.25 |
| 20/1 | Pumice B-2 | 67.43 | 0.46 | 12.50 | 5.00 | 0.23 | 0.14 | 0.63 | 3.45 | 6.39 | 96.23 |
| 21/1 | | 68.36 | 0.52 | 12.28 | 5.19 | 0.24 | 0.03 | 0.59 | 3.57 | 6.43 | 97.20 |
| 22/1 | | 67.91 | 0.47 | 12.66 | 5.07 | 0.25 | 0.13 | 0.51 | 4.31 | 5.62 | 96.92 |
| 23/1 | | 69.42 | 0.45 | 11.94 | 5.00 | 0.30 | 0.16 | 0.49 | 4.54 | 5.25 | 97.54 |
| 24/1 | | 68.97 | 0.51 | 11.76 | 5.19 | 0.24 | 0.17 | 0.52 | 4.19 | 5.74 | 97.29 |
| | Average | 68.42 | 0.48 | 12.23 | 5.09 | 0.25 | 0.12 | 0.55 | 4.01 | 5.88 | 97.04 |
| | SD | 0.80 | 0.03 | 0.37 | 0.10 | 0.03 | 0.05 | 0.06 | 0.47 | 0.51 | 0.50 |
| 27/1 | Pumice B-3 | 73.23 | 0.30 | 9.87 | 4.55 | 0.12 | 0.05 | 0.18 | 4.10 | 4.89 | 97.28 |
| 28/1 | | 73.13 | 0.30 | 9.93 | 4.81 | 0.20 | 0.02 | 0.18 | 4.09 | 5.21 | 97.86 |
| 29/1 | | 72.68 | 0.26 | 9.99 | 4.45 | 0.17 | 0.00 | 0.22 | 4.05 | 5.13 | 96.95 |
| 30/1 | | 71.61 | 0.29 | 9.21 | 4.66 | 0.21 | 0.09 | 0.21 | 4.10 | 4.94 | 95.33 |
| 31/1 | | 73.14 | 0.25 | 9.84 | 4.65 | 0.19 | 0.02 | 0.19 | 4.04 | 4.95 | 97.27 |
| 32/1 | | 72.98 | 0.31 | 9.87 | 4.57 | 0.20 | 0.02 | 0.24 | 4.11 | 4.94 | 97.24 |
| | Average | 72.79 | 0.28 | 9.79 | 4.62 | 0.18 | 0.03 | 0.20 | 4.08 | 5.01 | 96.99 |
| | SD | 0.61 | 0.02 | 0.29 | 0.12 | 0.04 | 0.03 | 0.02 | 0.03 | 0.13 | 0.87 |
| 34/1 | Pumice B-4 | 73.20 | 0.25 | 9.41 | 4.81 | 0.06 | 0.00 | 0.17 | 4.32 | 4.79 | 97.00 |
| 35/1 | | 71.81 | 0.29 | 9.48 | 5.23 | 0.17 | 0.00 | 0.14 | 4.29 | 4.88 | 96.29 |
| 36/1 | | 73.12 | 0.27 | 9.37 | 5.09 | 0.22 | 0.02 | 0.17 | 4.37 | 4.49 | 97.11 |
| 37/1 | | 71.64 | 0.28 | 9.21 | 5.06 | 0.13 | 0.03 | 0.17 | 3.80 | 5.45 | 95.76 |
| 38/1 | | 72.13 | 0.27 | 9.40 | 4.93 | 0.16 | 0.07 | 0.21 | 3.86 | 5.31 | 96.33 |
| | Average | 72.38 | 0.27 | 9.37 | 5.02 | 0.15 | 0.02 | 0.17 | 4.13 | 4.98 | 96.50 |
| | SD | 0.73 | 0.01 | 0.10 | 0.16 | 0.06 | 0.03 | 0.02 | 0.27 | 0.40 | 0.56 |
| 39/1 | Pumice B-5 | 71.41 | 0.29 | 10.93 | 5.10 | 0.15 | 0.00 | 0.17 | 4.53 | 5.52 | 98.09 |
| 40/1 | | 70.56 | 0.37 | 10.61 | 4.57 | 0.20 | 0.10 | 0.25 | 4.39 | 5.41 | 96.44 |
| 41/1 | | 70.28 | 0.34 | 10.83 | 4.51 | 0.19 | 0.06 | 0.23 | 4.28 | 5.94 | 96.66 |
| 42/1 | | 71.45 | 0.29 | 10.77 | 4.76 | 0.23 | 0.04 | 0.21 | 4.22 | 5.75 | 97.72 |
| 43/1 | | 70.08 | 0.35 | 10.98 | 4.92 | 0.28 | 0.07 | 0.37 | 3.97 | 5.76 | 96.78 |
| | Average | 70.76 | 0.33 | 10.82 | 4.77 | 0.21 | 0.05 | 0.24 | 4.28 | 5.68 | 97.14 |
| | SD | 0.64 | 0.04 | 0.14 | 0.25 | 0.05 | 0.04 | 0.08 | 0.21 | 0.21 | 0.72 |
| 47/1 | Pumice B-6 | 71.98 | 0.24 | 9.74 | 4.83 | 0.22 | 0.08 | 0.18 | 3.81 | 5.28 | 96.36 |
| 48/1 | | 72.58 | 0.35 | 10.15 | 4.68 | 0.11 | 0.07 | 0.07 | 3.79 | 5.71 | 97.51 |
| 49/1 | | 72.26 | 0.26 | 10.01 | 4.63 | 0.17 | 0.03 | 0.15 | 3.57 | 5.84 | 96.91 |
| 50/1 | | 73.80 | 0.36 | 9.39 | 5.46 | 0.09 | 0.00 | 0.06 | 4.12 | 5.03 | 98.31 |
| 51/1 | | 71.76 | 0.26 | 9.81 | 5.12 | 0.20 | 0.01 | 0.10 | 3.57 | 5.44 | 96.27 |
| | Average | 72.48 | 0.29 | 9.82 | 4.94 | 0.16 | 0.04 | 0.11 | 3.77 | 5.46 | 97.07 |
| | SD | 0.80 | 0.05 | 0.29 | 0.35 | 0.06 | 0.03 | 0.05 | 0.23 | 0.33 | 0.85 |
| 1/1 | Pumice A-1 | 73.10 | 0.29 | 9.96 | 4.45 | 0.19 | 0.00 | 0.25 | 4.07 | 5.06 | 97.36 |
| 2/1 | | 73.96 | 0.26 | 10.01 | 4.58 | 0.21 | 0.00 | 0.18 | 3.91 | 5.18 | 98.28 |
| 3/1 | | 73.60 | 0.26 | 9.63 | 4.56 | 0.22 | 0.01 | 0.19 | 4.09 | 4.92 | 97.48 |

**Table 2** continued

| Spot | Material | $SiO_2$ (%) | $TiO_2$ (%) | $Al_2O_3$ (%) | $Fe_2O_3$ (%) | MnO (%) | MgO (%) | CaO (%) | $Na_2O$ (%) | $K_2O$ (%) | Totals |
|---|---|---|---|---|---|---|---|---|---|---|---|
| 4/1 | | 73.34 | 0.29 | 9.74 | 4.26 | 0.19 | 0.00 | 0.18 | 4.08 | 5.01 | 97.08 |
| 5/1 | | 73.31 | 0.25 | 9.59 | 4.95 | 0.07 | 0.00 | 0.17 | 4.06 | 5.01 | 97.42 |
| 6/1 | | 73.46 | 0.29 | 9.88 | 4.90 | 0.20 | 0.00 | 0.21 | 4.05 | 5.00 | 97.97 |
| 7/1 | | 72.55 | 0.31 | 9.69 | 4.43 | 0.26 | 0.00 | 0.20 | 3.98 | 5.27 | 96.69 |
| 8/1 | | 72.74 | 0.20 | 9.53 | 4.59 | 0.19 | 0.02 | 0.19 | 4.03 | 5.29 | 96.78 |
| | Average | 73.26 | 0.27 | 9.75 | 4.59 | 0.19 | 0.00 | 0.19 | 4.03 | 5.09 | 97.38 |
| | SD | 0.46 | 0.03 | 0.18 | 0.23 | 0.05 | 0.01 | 0.02 | 0.06 | 0.14 | 0.55 |
| 10/1 | Pumice A-2 | 70.05 | 0.42 | 12.15 | 5.01 | 0.15 | 0.07 | 0.42 | 4.66 | 5.46 | 98.39 |
| 11/1 | | 70.74 | 0.39 | 11.02 | 4.83 | 0.28 | 0.09 | 0.46 | 4.44 | 5.28 | 97.54 |
| 12/1 | | 71.26 | 0.36 | 10.79 | 4.92 | 0.18 | 0.07 | 0.37 | 4.58 | 5.22 | 97.75 |
| 13/1 | | 71.16 | 0.38 | 10.87 | 4.87 | 0.18 | 0.00 | 0.22 | 4.52 | 5.62 | 97.83 |
| | Average | 70.80 | 0.39 | 11.21 | 4.91 | 0.20 | 0.06 | 0.37 | 4.55 | 5.40 | 97.88 |
| | SD | 0.55 | 0.02 | 0.64 | 0.08 | 0.06 | 0.04 | 0.10 | 0.10 | 0.18 | 0.37 |
| 14/1 | Pumice A-3 | 68.53 | 0.45 | 11.69 | 5.04 | 0.23 | 0.18 | 0.45 | 4.60 | 5.58 | 96.76 |
| 15/1 | | 69.55 | 0.42 | 11.83 | 5.13 | 0.20 | 0.19 | 0.54 | 4.57 | 5.33 | 97.76 |
| 16/1 | | 71.66 | 0.40 | 11.64 | 5.02 | 0.23 | 0.08 | 0.38 | 4.26 | 5.31 | 98.98 |
| 17/1 | | 67.82 | 0.50 | 12.51 | 5.14 | 0.30 | 0.22 | 0.59 | 4.64 | 5.53 | 97.25 |
| | Average | 69.39 | 0.44 | 11.92 | 5.08 | 0.24 | 0.17 | 0.49 | 4.52 | 5.44 | 97.69 |
| | SD | 1.67 | 0.04 | 0.40 | 0.06 | 0.04 | 0.06 | 0.09 | 0.18 | 0.14 | 0.95 |
| 18/1 | Pumice A-4 | 71.50 | 0.38 | 10.79 | 4.99 | 0.25 | 0.05 | 0.39 | 4.57 | 5.28 | 98.19 |
| 19/1 | | 73.22 | 0.31 | 10.53 | 4.89 | 0.17 | 0.00 | 0.06 | 4.17 | 5.13 | 98.47 |
| 20/1 | | 70.87 | 0.34 | 10.87 | 4.36 | 0.16 | 0.08 | 0.23 | 3.14 | 5.82 | 95.87 |
| | Average | 71.86 | 0.34 | 10.73 | 4.75 | 0.19 | 0.05 | 0.23 | 3.96 | 5.41 | 97.51 |
| | SD | 1.21 | 0.03 | 0.18 | 0.34 | 0.05 | 0.04 | 0.17 | 0.74 | 0.36 | 1.43 |
| 21/1 | Pumice A-5 | 73.59 | 0.28 | 10.22 | 4.82 | 0.17 | 0.00 | 0.20 | 4.06 | 5.25 | 98.59 |
| 22/1 | | 72.44 | 0.22 | 9.85 | 4.66 | 0.09 | 0.04 | 0.17 | 3.97 | 5.43 | 96.86 |
| 23/1 | | 72.58 | 0.34 | 9.83 | 4.62 | 0.17 | 0.01 | 0.16 | 4.05 | 5.09 | 96.86 |
| 24/1 | | 71.27 | 0.34 | 9.98 | 4.78 | 0.18 | 0.00 | 0.22 | 4.18 | 5.25 | 96.20 |
| | Average | 72.47 | 0.30 | 9.97 | 4.72 | 0.15 | 0.01 | 0.19 | 4.06 | 5.25 | 97.12 |
| | SD | 0.95 | 0.06 | 0.18 | 0.09 | 0.04 | 0.02 | 0.02 | 0.09 | 0.14 | 1.02 |
| 25/1 | Pumice A-6 | 72.75 | 0.28 | 10.21 | 4.65 | 0.21 | 0.02 | 0.21 | 4.08 | 5.56 | 97.97 |
| 26/1 | | 72.39 | 0.34 | 10.43 | 4.80 | 0.20 | 0.00 | 0.21 | 4.25 | 5.24 | 97.85 |
| 27/1 | | 71.53 | 0.32 | 10.36 | 4.79 | 0.20 | 0.04 | 0.24 | 3.97 | 5.53 | 96.98 |
| 28/1 | | 71.80 | 0.26 | 10.35 | 4.79 | 0.19 | 0.01 | 0.20 | 4.21 | 5.11 | 96.90 |
| | Average | 72.12 | 0.30 | 10.34 | 4.76 | 0.20 | 0.02 | 0.22 | 4.13 | 5.36 | 97.43 |
| | SD | 0.55 | 0.04 | 0.09 | 0.07 | 0.01 | 0.02 | 0.02 | 0.12 | 0.22 | 0.56 |
| 33/1 | Pumice A-7 | 68.35 | 0.55 | 13.09 | 5.03 | 0.24 | 0.19 | 0.61 | 4.51 | 5.76 | 98.32 |
| 34/1 | | 67.20 | 0.55 | 13.50 | 5.17 | 0.26 | 0.09 | 0.64 | 4.17 | 6.43 | 98.01 |
| 35/1 | | 66.12 | 0.51 | 13.11 | 5.48 | 0.31 | 0.18 | 0.75 | 4.66 | 6.13 | 97.26 |
| 36/1 | | 66.98 | 0.50 | 13.26 | 5.30 | 0.31 | 0.08 | 0.69 | 4.46 | 6.02 | 97.58 |
| 37/1 | | 67.12 | 0.56 | 13.70 | 4.97 | 0.28 | 0.12 | 0.68 | 4.13 | 6.83 | 98.38 |
| | Average | 67.16 | 0.53 | 13.33 | 5.19 | 0.28 | 0.13 | 0.67 | 4.39 | 6.23 | 97.91 |
| | SD | 0.80 | 0.03 | 0.26 | 0.21 | 0.03 | 0.05 | 0.05 | 0.23 | 0.41 | 0.48 |
| 38/1 | Pumice A-8 | 73.50 | 0.28 | 10.23 | 4.63 | 0.20 | 0.08 | 0.24 | 4.40 | 4.99 | 98.53 |
| 39/1 | | 71.50 | 0.28 | 10.31 | 4.85 | 0.17 | 0.06 | 0.22 | 4.45 | 5.11 | 96.96 |
| 40/1 | | 73.30 | 0.32 | 10.25 | 4.73 | 0.19 | 0.04 | 0.23 | 4.35 | 5.06 | 98.46 |
| 41/1 | | 73.27 | 0.27 | 9.80 | 4.58 | 0.17 | 0.00 | 0.22 | 4.20 | 4.90 | 97.40 |
| 42/1 | | 73.76 | 0.30 | 9.11 | 5.21 | 0.13 | 0.00 | 0.12 | 4.30 | 4.98 | 97.90 |

**Table 2** continued

| Spot | Material | $SiO_2$ (%) | $TiO_2$ (%) | $Al_2O_3$ (%) | $Fe_2O_3$ (%) | MnO (%) | MgO (%) | CaO (%) | $Na_2O$ (%) | $K_2O$ (%) | Totals |
|---|---|---|---|---|---|---|---|---|---|---|---|
| | Average | 73.07 | 0.29 | 9.94 | 4.80 | 0.17 | 0.03 | 0.21 | 4.34 | 5.01 | 97.85 |
| | SD | 0.90 | 0.02 | 0.51 | 0.25 | 0.03 | 0.03 | 0.05 | 0.10 | 0.08 | 0.68 |
| 45/1 | Pumice A-9 | 73.66 | 0.31 | 9.97 | 4.58 | 0.22 | 0.00 | 0.13 | 4.08 | 5.15 | 98.10 |
| 46/1 | | 73.43 | 0.21 | 9.95 | 4.48 | 0.20 | 0.00 | 0.13 | 3.44 | 5.83 | 97.67 |
| 47/1 | | 71.23 | 0.32 | 9.98 | 4.86 | 0.26 | 0.00 | 0.20 | 4.06 | 5.81 | 96.72 |
| 48/1 | | 73.36 | 0.26 | 9.56 | 4.80 | 0.11 | 0.02 | 0.15 | 4.06 | 5.29 | 97.59 |
| 49/1 | | 73.56 | 0.30 | 9.76 | 4.81 | 0.15 | 0.00 | 0.13 | 4.07 | 5.16 | 97.93 |
| | Average | 73.05 | 0.28 | 9.84 | 4.71 | 0.19 | 0.00 | 0.15 | 3.94 | 5.45 | 97.60 |
| | SD | 1.02 | 0.05 | 0.18 | 0.17 | 0.06 | 0.01 | 0.03 | 0.28 | 0.34 | 0.54 |
| 50/1 | Pumice A-10 | 70.52 | 0.40 | 10.30 | 4.84 | 0.21 | 0.02 | 0.34 | 4.30 | 5.55 | 96.48 |
| 51/1 | | 72.11 | 0.36 | 10.85 | 4.56 | 0.20 | 0.06 | 0.11 | 3.55 | 6.16 | 97.95 |
| | Average | 71.31 | 0.38 | 10.58 | 4.70 | 0.21 | 0.04 | 0.22 | 3.92 | 5.85 | 97.22 |
| | SD | 1.12 | 0.03 | 0.39 | 0.19 | 0.01 | 0.02 | 0.16 | 0.53 | 0.43 | 1.04 |
| 56/1 | Pumice A-11 | 70.75 | 0.39 | 11.30 | 4.77 | 0.14 | 0.04 | 0.09 | 4.31 | 5.78 | 97.57 |
| 57/1 | | 71.97 | 0.34 | 10.82 | 5.08 | 0.25 | 0.03 | 0.16 | 4.53 | 5.59 | 98.77 |
| 58/1 | | 71.23 | 0.30 | 10.92 | 4.84 | 0.13 | 0.05 | 0.13 | 4.57 | 5.26 | 97.42 |
| 59/1 | | 70.92 | 0.32 | 11.34 | 4.55 | 0.22 | 0.07 | 0.19 | 3.90 | 6.26 | 97.78 |
| | Average | 71.22 | 0.34 | 11.09 | 4.81 | 0.18 | 0.05 | 0.14 | 4.33 | 5.72 | 97.89 |
| | SD | 0.54 | 0.04 | 0.26 | 0.22 | 0.06 | 0.02 | 0.04 | 0.31 | 0.42 | 0.61 |
| 60/1 | Pumice A-12 | 66.54 | 0.59 | 13.31 | 4.99 | 0.16 | 0.15 | 0.52 | 4.49 | 6.28 | 97.04 |
| 61/1 | | 69.76 | 0.37 | 10.81 | 5.20 | 0.28 | 0.19 | 0.30 | 3.51 | 6.54 | 96.96 |
| 62/1 | | 67.59 | 0.47 | 12.11 | 5.10 | 0.24 | 0.19 | 0.67 | 4.36 | 5.43 | 96.16 |
| 63/1 | | 69.08 | 0.51 | 12.48 | 4.99 | 0.22 | 0.20 | 0.64 | 4.10 | 6.28 | 98.50 |
| | Average | 68.24 | 0.49 | 12.18 | 5.07 | 0.23 | 0.18 | 0.53 | 4.11 | 6.13 | 97.16 |
| | SD | 1.45 | 0.09 | 1.04 | 0.10 | 0.05 | 0.02 | 0.17 | 0.43 | 0.49 | 0.97 |
| 53/1 | Shard A-1 | 73.55 | 0.28 | 10.23 | 4.92 | 0.17 | 0.02 | 0.19 | 3.53 | 5.52 | 98.41 |
| 64/1 | Shard A-2 | 72.08 | 0.25 | 9.35 | 4.82 | 0.13 | 0.02 | 0.18 | 3.97 | 4.93 | 95.74 |
| 65/1 | Shard A-3 | 73.64 | 0.25 | 9.47 | 4.78 | 0.17 | 0.02 | 0.09 | 4.02 | 5.30 | 97.73 |
| 69/1 | Shard A-4 | 74.67 | 0.27 | 9.54 | 4.66 | 0.13 | 0.04 | 0.18 | 4.13 | 5.13 | 98.73 |
| 25/1 | Shard B-1 | 71.73 | 0.30 | 9.43 | 4.76 | 0.17 | 0.01 | 0.18 | 4.08 | 4.62 | 95.28 |
| 33/1 | Shard B-2 | 73.28 | 0.26 | 9.86 | 4.74 | 0.21 | 0.00 | 0.19 | 4.24 | 5.22 | 97.99 |

Analytical details are outlined in the online supplemental materials

## Discussion

### Petrogenesis of Chefe Donsa Magmas

While some evidence of magma mingling is preserved within the Chefe Donsa glasses, it is unlikely that mixing processes could have generated the wide array of compositions evident in the unmingled pumice. In particular, the hyperbolic trends evident for most incompatible trace elements and the behavior of Eu preclude simple end-member mixing in generating the range of compositions observed. Deriving the liquid line of descent and ultimate origin of peralkaline magmas remains a controversial issue, with at least three competing models: (A) fractionation of mildly alkaline (or transitional) magmas (e.g., Barberi et al. 1975); (B) partial melting of the continental crust (e.g., MacDonald et al. 1987); and (C) a two-step processes involving partial melting of crustal rocks/cumulates followed by crystal fractionation of the resulting liquid (e.g., Avanzinelli et al. 2004). Previous studies in the region investigating the nearby silicic centers at Debre Zeyit found that most silicic magmas are the result of fractional crystallization from parental basaltic liquids (Gasparon et al. 1993), consistent with interpretations for the origin of rhyolites throughout the region (e.g., Ayalew 2011; Ayalew and Ishiwatari 2011). The very low concentrations of Ba and Sr and low values of Rb/Nb (<1.34) and La/Nb (<1.1) present in the Chefe Donsa pumice could not be produced by anatexis of typical crustal lithologies (Pearce et al. 1984; Heumann and Davies 2002; MacDonald and

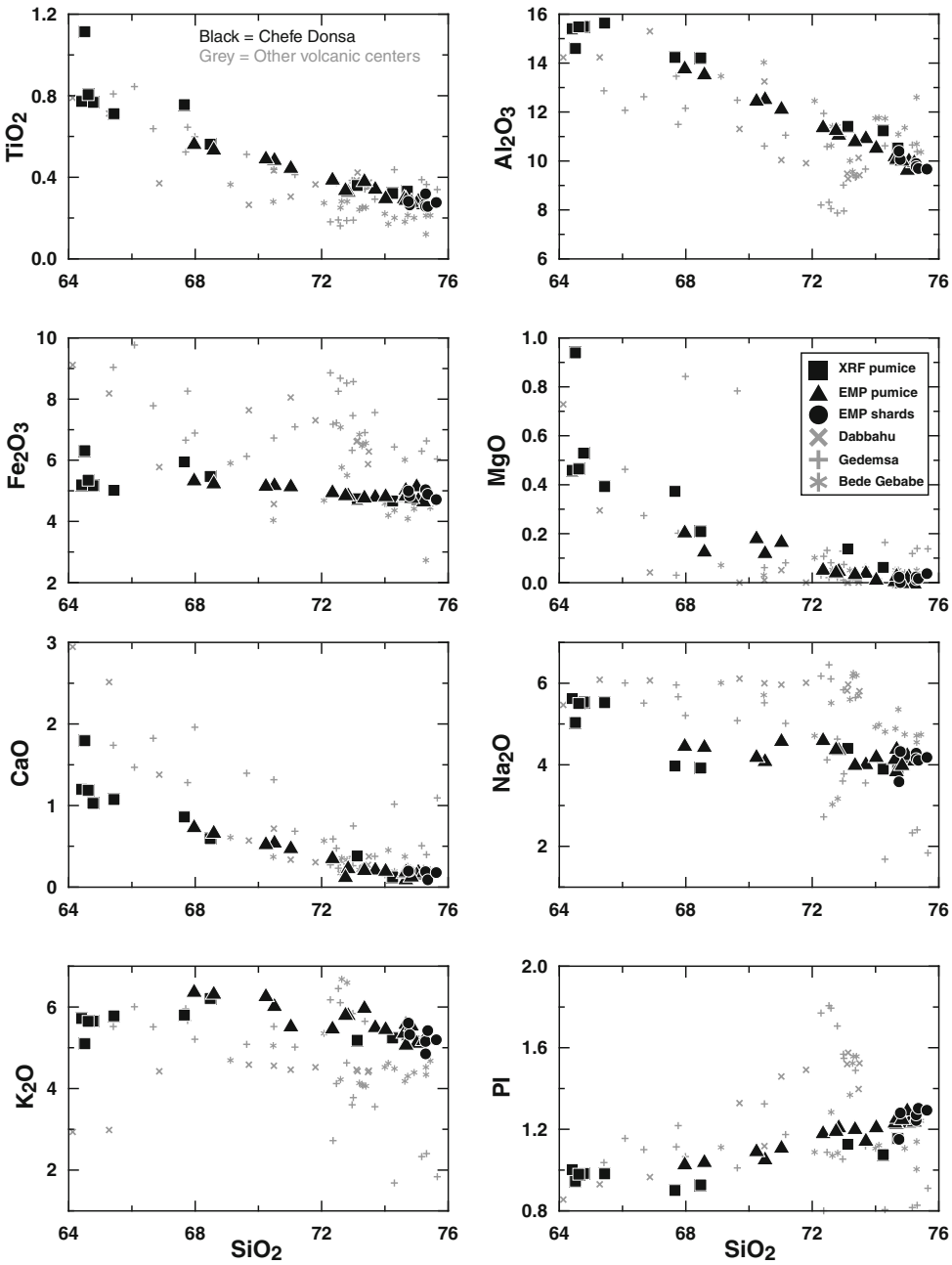


**Fig. 2** Major element variation as a function of silica. All values are wt%. Chefe Donsa data divided into **a** XRF data on whole-pumice clasts, **b** Electron microprobe (EMP) data on glass within pumice fragments, **c** EMP data on glass shards hosted within the ash. Shown for comparison in *gray* are data from other peralkaline centers in the Ethiopian Rift and Afar: Dabbahu (Boina) (Barberi et al. 1975); Gedemsa (Peccerillo et al. 2003); Bede Gebebe (Gasparon et al. 1993). The peralkalinity index (PI) is calculated as (Na + K)/Al. Iron is presented as $Fe_2O_3$ (total)

Scaillet 2006) and are consistent with the hypothesis that the Chefe Donsa peralkaline magmas are derived by assimilation and fractional crystallization processes.

To examine the possible differentiation sequence at Chefe Donsa, we have undertaken modeling of potential parental basalt compositions using Rhyolite-MELTS (Gualda et al. 2012)—a revised formulation of the MELTS thermodynamic modeling suite (Ghiorso and Sack 1995) that more accurately represents quartz and alkali feldspar stability relations. Two variably contaminated primitive basalts from the nearby Pliocene Akaki chain (samples 2015 and 2024) were selected as parental compositions for a series of fractional crystallization models with various values of oxidation state, water content, and pressure (Fig. 7). The basalts of the Akaki chain may not be strictly related to the Chefe Donsa parental magmas; however, they represent the closest spatial and temporal mafic magmas to the Chefe Donsa caldera. The results of this modeling show that the potential fractionation paths for sample 2015 more closely resemble the variation observed in the Chefe Donsa suite (Fig. 7). In particular, close agreement between the modeled and observed values is seen for $K_2O$, $Na_2O$, and $SiO_2$. The primary distinction between the two model inputs was the elevated values of $SiO_2$, $K_2O$, and low

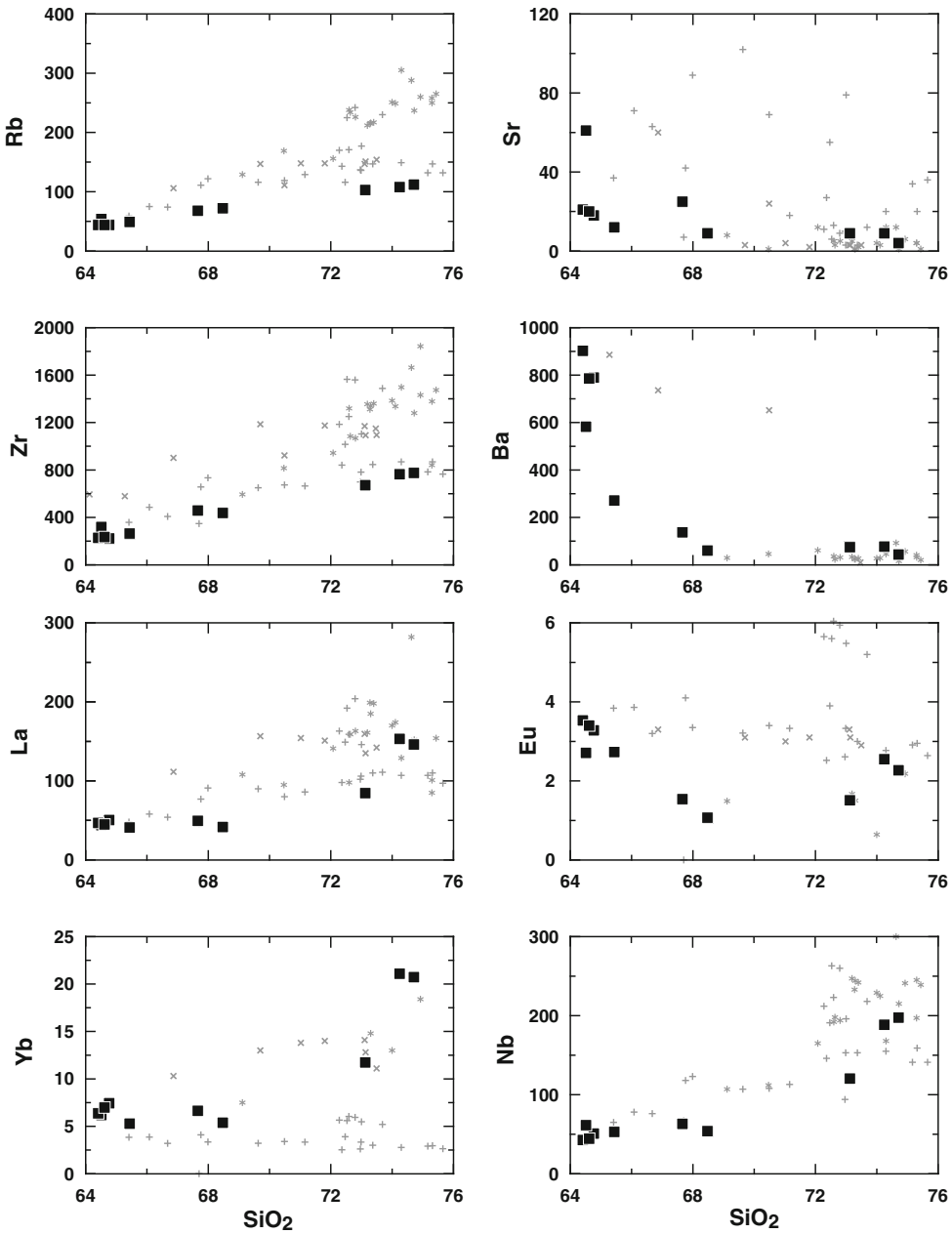


**Fig. 3** Trace element variation as a function of silica. Trace elements are reported as parts per million; $SiO_2$ is reported as wt%. Data sources are the same as in Fig. 2

Ce/Pb observed in sample 2015 in comparison with 2024 (Fig. 7). The chemical differences between these samples are most probably related to some degree of crustal assimilation or mixing with a more evolved magma in sample 2015. These results suggest that some degree of assimilation/mixing is important for the generation of the Chefe Donsa peralkaline suite, consistent with models for the genesis of peralkaline rhyolites from the nearby Gedemsa Caldera (Peccerillo et al. 2003). Fractionation paths at medium to lower pressures (<5,000 bars) best fit the observed data.

A significant inconsistency in CaO and $P_2O_5$ between the modeled MELTS liquids and the observed variability in the Chefe Donsa pumice requires further investigation. To establish whether the observed CaO and $P_2O_5$ anomalies are related to the selection of parental material, we undertook MELTS modeling using the more primitive endmembers from the Chefe Donsa pumice as a starting composition (Fig. 8a). This modeling reveals that the magma represented by the most evolved pumice fragments (~75 % $SiO_2$) can be derived from the most primitive pumice (~64 % $SiO_2$) by ~70 % fractional crystallization of an assemblage dominated by alkali feldspar (~90 %) with minor contributions from olivine, spinel, orthopyroxene, and oxides at low pressures (~500 bars). Some variability in the slopes of modeled $TiO_2$ and FeO in

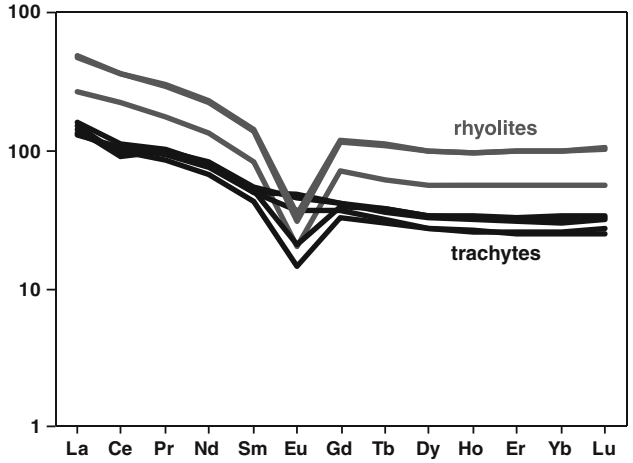


**Fig. 4** Chefe Donsa data normalized to C1 chondrite values of Boynton et al. (1984)

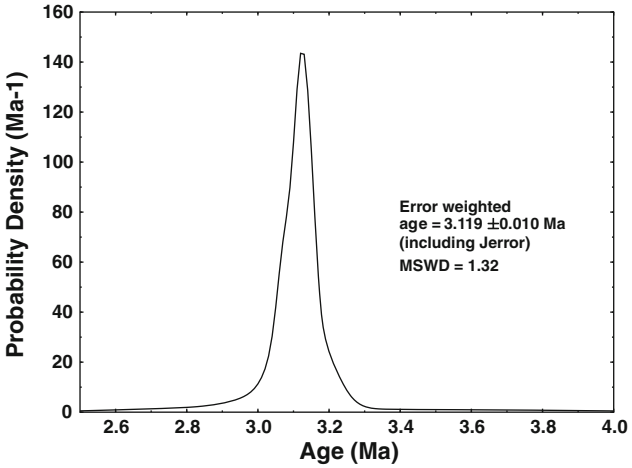


**Fig. 6** Sample 2012A single-crystal Gaussian histogram. See text for detailed "Discussion"

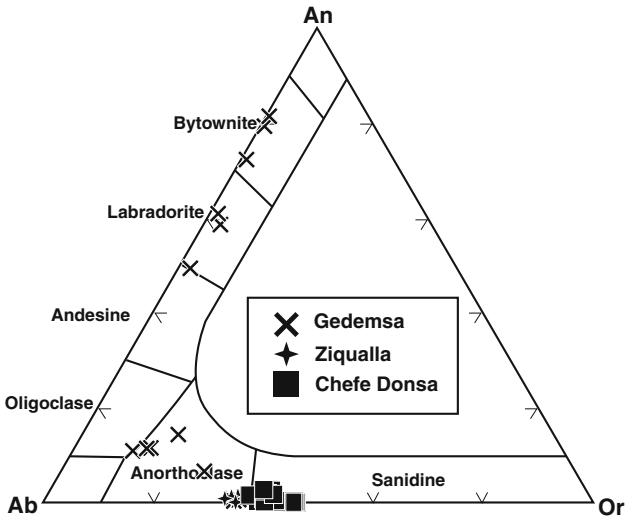


**Fig. 5** Feldspar compositions for Chefe Donsa and other nearby silicic centers: Ziqualla (Gasparon et al. 1993); Gedemsa (Peccerillo et al. 2003)

comparison with the observed values likely reflects the role of Fe-Ti oxides and aenigmatite ($Na_2Fe_5TiO_2[Si_6O_{18}]$); however, the most significant discordance between the observed and modeled results was for CaO and $P_2O_5$, which consistently rose with increasing $SiO_2$, while observed values in the Chefe Donsa pumice fell, despite adjustments to the oxidation state, pressure, and water content of the modeled system (Fig. 8a). This phenomenon is not localized to the Chefe Donsa system, and similar inconsistencies arise between modeled and observed CaO and $P_2O_5$ values for other peralkaline systems such as the Dabbahu (Boina) center and Gedemsa Caldera (Fig. 8b). The commonality of CaO and $P_2O_5$ inconsistencies in these peralkaline systems may relate to the stabilization and fractionation of flour-apatite, a phase not currently accounted for in the MELTS formulation.

The stability of phases in peralkaline systems has been recently explored by experimental methods, though the stability of apatite was not assessed (Scaillet and MacDonald 2001, 2003). These studies concluded that as a system becomes peralkaline, plagioclase crystallization is immediately suppressed and that phases with a significant F component (e.g., amphibole) will have a much wider stability range. Igneous apatite $Ca_5(PO_4)_3(F, Cl, OH)$ has a significant F component, and indeed, flour-apatite is typically the most abundant apatite endmember in igneous systems (Deer et al. 1996). The current MELTS formulation accounts only for hydroxyl-apatite stability relations with variations in system $H_2O$ content. The residual liquids in the Rhyolite-MELTS fractionation results displayed in Figs. 7, 8 saturate with hydroxyl-apatite at ~60 wt% $SiO_2$, but despite its saturation, insufficient amounts of the phase are removed from the system to correctly model the CaO and $P_2O_5$ fractionation trends observed in the lavas. If, as is likely, the stability field of apatite is greatly enhanced by the incorporation of fluorine, it would require a system concentration of approximately 675 ppm F to quantitatively bring the modeled residual CaO and $P_2O_5$ liquid concentrations into agreement with those trends observed in the rocks (Fig. 8b). This required concentration of F is consistent with the values reported in compositionally similar rocks from the nearby Gedemsa volcano (92–3,138 ppm: Yirgu et al. 1999). Assuming the mismatch between the modeled and observed $P_2O_5$ is the result of apatite fractionation, ~1.4–2.4 % apatite (0.44–0.75 % of the total system) removal is required (see supplemental data for details). The removal of this apatite would reduce modeled CaO values to ~0.8–0.9 %, still higher than observed value of 0.1 %; however, Si–P substitutions in the

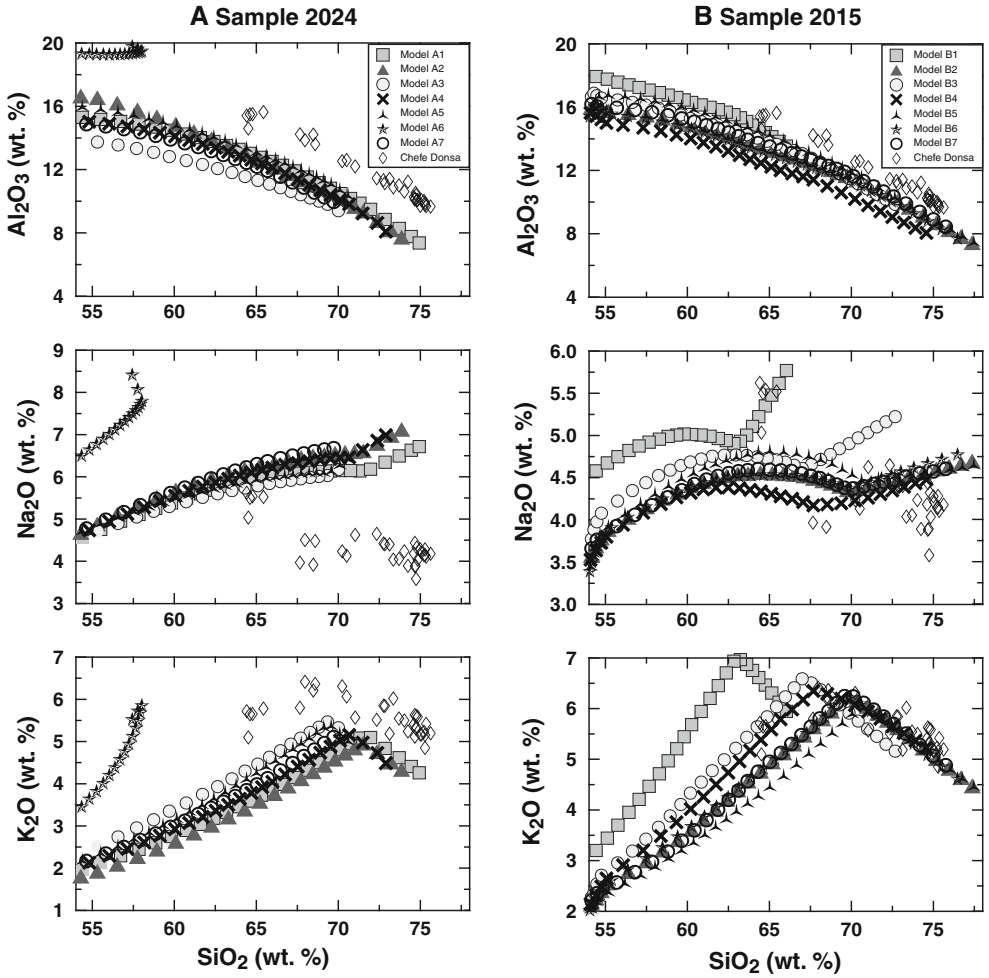


**Fig. 7** Model results from thermodynamic modeling using Rhyolite-MELTS. All Rhyolite-MELTS models were run under a 'fractionate solids' flag. Oxidation state was not constrained but initial $Fe^{2+}/Fe^{3+}$ was estimated using a range of values from QFM−1 to QFM+1. Ranges chosen are consistent with previous studies (e.g., Peccerillo et al. 2003; Rooney et al. 2007; Rooney 2010). **a** Model A1—QFM+1, 500 bars, 0.5 % $H_2O$; Model A2—QFM, 500 bars, 1 % $H_2O$; Model A3—QFM, 500 bars, 0.2 % $H_2O$; Model A4—QFM, 500 bars, 0.5 % $H_2O$; Model A5—QFM, 2000 bars, 0.5 % $H_2O$; Model A6—QFM, 5000 bars, 0.5 % $H_2O$; Model A7—QFM−1, 500 bars, 0.5 % $H_2O$. **b** Model B1—QFM, 5000 bars, 0.5 % $H_2O$; Model B2—QFM, 500 bars, 0.5 % $H_2O$; Model B3—QFM, 2000 bars, 0.5 % $H_2O$; Model B4—QFM, 500 bars, 0.2 % $H_2O$; Model B5—QFM, 500 bars, 1 % $H_2O$; Model B6—QFM−1, 500 bars, 0.5 % $H_2O$; Model B7—QFM+1, 500 bars, 0.5 % $H_2O$

apatite *Z* site (MacDonald et al. 2008) may impact P/Ca, and the exact composition of apatite in the Chefe Donsa system remains unknown. We surmise that it is probable that the observed mismatch between MELTS-modeled and observed CaO and $P_2O_5$ liquid trends relates to the stabilization effect of F on apatite.

To investigate the role of apatite in the Chefe Donsa magmatic system, we performed a least-squares fit (weighted for $P_2O_5$ and CaO) between more primitive (∼65 % $SiO_2$) and evolved pumice fragments (∼75 % $SiO_2$) using mineral compositions from Chefe Donsa and from other peralkaline systems (see supplementary data). The outcome of this model is broadly consistent with the thermodynamic results and predicts ∼0.7 % apatite removal accompanied by other solids that are dominated by alkali feldspar (∼92 %). Using these least-squares results on the major elements and apatite/glass values from the Olkaria volcanic complex (MacDonald et al. 2008), we also examined the impact of this fractionating assemblage on the rare earth elements and Y. The modeled trace element evolution of the Chefe Donsa system is clearly erroneous and implies that the partition coefficient values selected for apatite may have been inappropriate. Partition coefficient data for apatite in peralkaline systems are sparse, so we have undertaken an inverse model assuming the mineral modes from our least-squares modeling, and have calculated the apparent D values for rare earth elements in apatite for the Chefe Donsa system (see supplementary data). These calculated D values peak at Sm, consistent with measured apatite D values, though the low

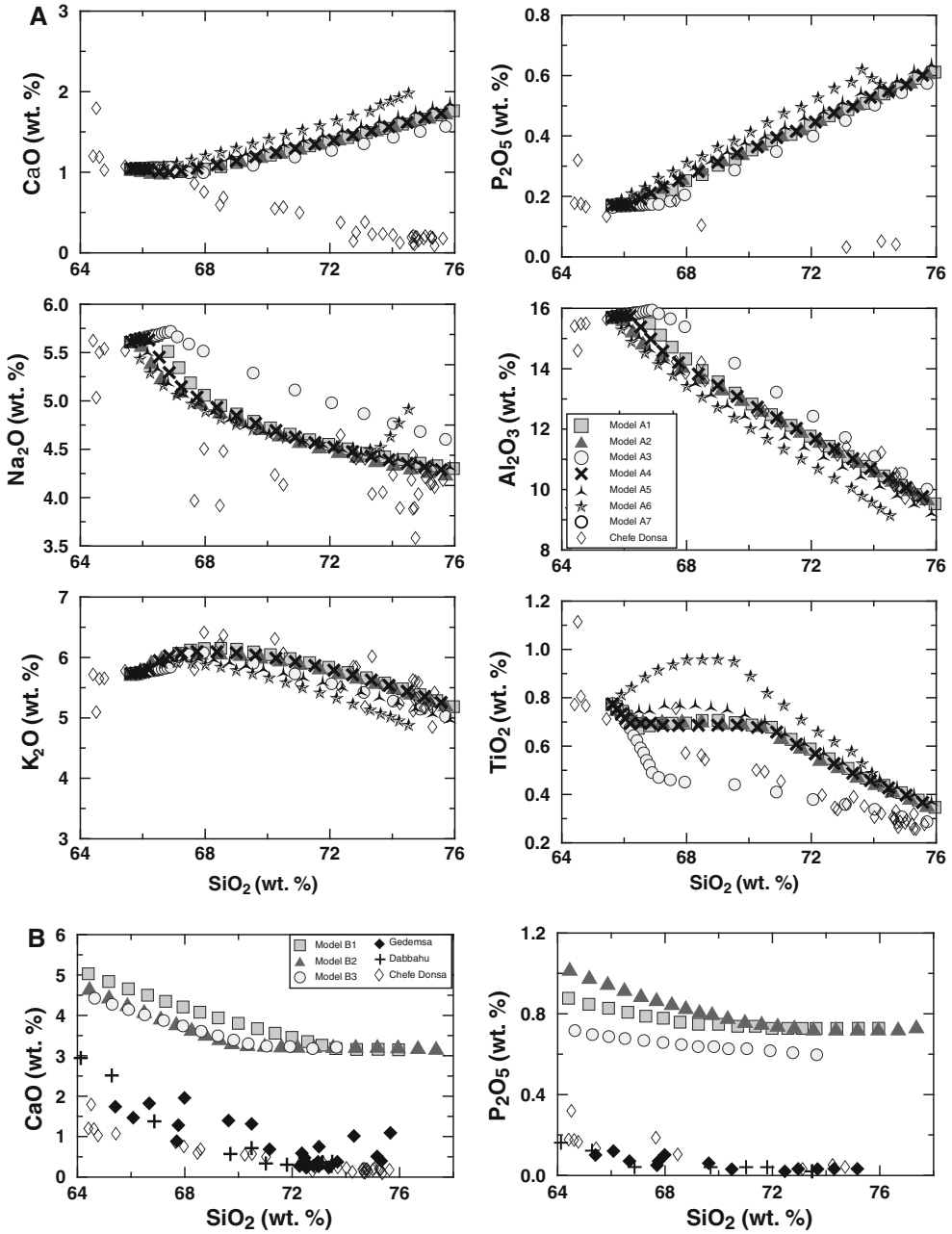


**Fig. 8** Model results from thermodynamic modeling using Rhyolite-MELTS. All Rhyolite-MELTS models were run under a 'fractionate solids' flag. Oxidation state was not constrained but initial $Fe^{2+}/Fe^{3+}$ was estimated using a range of values from QFM−1 to QFM+1. **a** Model A1—QFM+1, 500 bars, 0.5 % $H_2O$; Model A2—QFM−1, 500 bars, 0.5 % $H_2O$; Model A3—QFM, 500 bars, 0.2 % $H_2O$; Model A4—QFM, 500 bars, 0.5 % $H_2O$; Model A5—QFM, 2000 bars, 0.5 % $H_2O$; Model A6—QFM, 5000 bars, 0.5 % $H_2O$. **b** Model B1—Sample GD65-Gedemsa, QFM, 500 bars, 0.5 % $H_2O$; Model B2—Sample 2015, QFM, 500 bars, 0.5 % $H_2O$; Model B3—Sample G495-Dabbahu (Boina), QFM, 500 bars, 0.5 % $H_2O$. Data for Gedemsa (Peccerillo et al. 2003) and Dabbahu (Boina) (Barberi et al. 1975) are shown for comparison

value for Ce is notable. The origin of the mismatch between our modeled D values and those measured from the Olkaria volcanic complex remains uncertain; though, it may relate to the particularly rare-earth-element-enriched nature of apatites in the Olkaria complex (several weight percent of rare earth elements occupying the apatite *M* site). Large contributions of rare earth elements to the apatite structure may limit the utility of partition coefficients to describe the behavior of these elements under such conditions. These results highlight the still uncertain role of halogens in controlling the fractionating assemblage in peralkaline systems (e.g., Rooney et al. 2010), and

further question the precise impact of apatite on the geochemical evolution of such systems.

## Magma chamber processes (mingling, pumice size, limited crystals)

This study, which focuses on a single eruptive episode of one silicic magmatic system, uniquely probes magma chamber processes in the Ethiopian Rift. We have shown that the geochemical characteristics of the Chefe Donsa pumice are unlikely to have been derived by crustal anatexis, highlighting the role of assimilation and fractional crystallization processes in generating the array of glass compositions observed. The contamination inferred for the basaltic parent of the Chefe Donsa magmas may have been the result of hybridization in a lower crustal hot zone (e.g., Annen and Sparks 2002; Annen et al. 2006), although our modeled crystallization paths for the evolution of the Chefe Donsa magmas imply that the majority of the differentiation process occurred in the mid-upper crust. The crystal-poor and high-viscosity characteristics of silicic magmas such as those at Chefe Donsa are increasingly interpreted utilizing a crystal mush and interstitial melt extraction model (Bachmann and Bergantz 2008; Dufek and Bachmann 2010; Deering et al. 2011b). This model hypothesizes that crystal-poor silicic melts may be efficiently extracted once a 'quasi-rigid crystalline skeleton' is generated at about 50–60 % crystallinity (Bachmann and Bergantz 2004, 2008; Deering et al. 2011a). Eruptibility of these extracted magmas then depends on vapor saturation; in relatively dry environments such as a continental rift, this may lead to bimodality of erupted compositions where intermediate magmas will not reach vapor saturation, but more evolved compositions will become saturated and erupt.

Such models have potential application in understanding the magmatic plumbing system of the Chefe Donsa and other peralkaline centers in the Ethiopian Rift. Pliocene to recent magmatism in the Ethiopian Rift is dominated by bimodal systems of large central silicic complexes and chains of smaller basaltic cinder cones (Rooney et al. 2011). These systems have been successfully modeled using a variety of thermodynamic and mass balance techniques (Trua et al. 1999; Peccerillo et al. 2003; Rooney et al. 2007). Starting with a mildly alkaline basalt, the range of magmatic products observed at the Gedemsa caldera may be successfully modeled by low-pressure fractionation at the QFM buffer, culminating in peralkaline magma compositions when about 10 % liquid remains (Peccerillo et al. 2003). Considering the permeability difficulties inherent to such a small liquid fraction, a mush-melt extraction model may be applicable. For our modeled parental composition (sample 2015), the 50–60 % crystallinity threshold for rheological locking is achieved when liquid compositions are ~61–64 % $SiO_2$ (similar to that modeled for Gedemsa: Peccerillo et al. 2003); melt extraction at this point would yield a liquid very similar in composition to the most primitive trachytic pumice observed at Chefe Donsa. This extracted trachytic magma will ascend and undergo continued crystal fractionation, resulting in the development of a second crystal mush at shallower levels within the crust (~500 bars; Fig. 8). Following a further 50–70 % crystallization of the trachytic magma, a rhyolite liquid similar in composition to the evolved pumice from Chefe Donsa could be released from this new mush. This conceptual model successfully addresses the difficulties of melt extraction in addition to explaining the lack of more primitive phenocryst compositions at Chefe Donsa, and is consistent with the results of our MELTS modeling that show the Chefe Donsa rhyolites can be derived from trachyte magmas following ~70 % crystallization at low pressures (~500 bars).

The array of geochemical compositions and mixing textures recorded at Chefe Donsa are consistent with studies of other East African peralkaline magmas that found pervasive magma mixing and zoning in magma chambers (e.g., MacDonald and Scaillet 2006). However, all analyzed materials at Chefe Donsa were derived from only two proximal samples recovered from close to one another, and therefore, it remains unclear if there is a vertical geochemical gradient (early versus later erupted materials). Some of the observed range in magmatic compositions in the Chefe Donsa deposit might result from the fresh intrusion of trachyte that may also have acted as the trigger for the eruption in a similar fashion to other magmatic systems (e.g., Sparks et al. 1977; Pallister et al. 1992; Nakamura 1995; Murphy et al. 2000; Ruprecht and Bachmann 2010).

## Tectonic implications

The Chefe Donsa caldera lies along the alignment of the Silti-Debre Zeyit Fault Zone and therefore provides insights into the development of a zone of focused magmatic intrusion. Extensive analysis of rift propagation processes in Afar has shown that large central silicic volcanoes (many stacked flows of silicic lavas) are emplaced prior to the propagation of a rift zone, and it is hypothesized that central silicic volcanoes may 'capture' the propagating rift by generating weaker lithosphere (van Wyk de Vries and Merle 1998; Lahitte et al. 2003). Continued extension leads to the disassembly of these central silicic volcanoes by faulting and the eruption of more basaltic magmas as crustal residence time drops (Lahitte et al. 2003). Existing studies of the Wonji Fault Belt and Silti-Debre Zeyit Fault Zone are consistent with this model

and have shown that while silicic and basaltic activity in the modern rift valley is largely contemporaneous (Peccerillo et al. 2003), dominantly silicic activity preceded the development of these bimodal associations (Morton et al. 1979; Wolfenden et al. 2004). The Chefe Donsa tephra at 3.119 Ma is within the temporal range of other silicic volcanoes in the Debre Zeyit region (Morton et al. 1979; Zanettin et al. 1979), but likely predates the basaltic activity (Mohr 1961), consistent with rift propagation models (e.g., Lahitte et al. 2003). The Chefe Donsa caldera differs from other silicic centers in the area (e.g., Bede Gebebe, Ziqualla) in that it is not composed of multiple flows, and remains undissected by later basaltic activity. It is likely that the position of the Chefe Donsa caldera on the thicker lithosphere of the Ethiopian plateau (Boru-Toru Structural high: Bonini et al. 2005) impeded rift propagation and extension (Buck 2004), minimizing subsequent magmatism at Chefe Donsa. This model is consistent with the hypothesized termination of the Silti-Debre Zeyit Fault Zone at the Chefe Donsa caldera (e.g., Rooney et al. 2011).

## Implications for the Tephra Record

Volcanic products often serve as essential stratigraphic marker horizons from which numerical age constraints and paleoenvironmental information for associated deposits may be derived (e.g., Sarna-Wojcicki et al. 1985). In dynamic environments such as the EARS, glass and/or mineral chemistry from the explosively erupted components (tephra) of magmatic systems often provide a robust means by which widely spaced depocenters and isolated sedimentary deposits can be correlated, including both continental rift basin and marine records (Sarna-Wojcicki et al. 1985; Brown et al. 1992; Hart et al. 1992; Woldegabriel et al. 2000; Feakins et al. 2007). While distal–distal tephra correlations historically have been a focus in the EARS, potential distal–proximal correlations have begun to receive greater attention (Hart et al. 1992; WoldeGabriel et al. 2005). These efforts have illustrated numerous difficulties in directly linking distal tephra to a specific eruptive center or eruptive event. This issue has been widely identified and is in part attributed to (1) differential preservation of materials from a single eruptive phase in the proximal and distal records, (2) complexities in the source magmatic system including pre-eruptive existence of multiple magma compositions and magma mingling, and 3) a lack of stratigraphic context and detailed sampling of potential source volcanoes (Perkins and Nash 2002; Shane et al. 2008). The Chefe Donsa proximal tephra data illustrate the importance of understanding the geochemical diversity in a single eruptive phase. These data also highlight the possible differential preservation of heterogeneous chemical signatures from a single eruption since the recovered glass shards, which are the most likely equivalents to what might be found in a distal deposit, display a very narrow compositional range compared to glass located within pumice fragments.

Ongoing investigations in the Middle Awash region and the Hadar region identify a sparse tephra record in the general age range of the Chefe Donsa eruption (Woldegabriel et al. 2000; Campisano and Feibel 2008; Roman et al. 2008; Hart and Woldegabriel 2010). Moreover, the ca. 3.1-Ma Chefe Donsa eruption occurs at a time that is poorly represented in the terrestrial and marine records that serve as archives for voluminous explosive eruptions from sources in the northern EARS (Feakins et al. 2007; Roman et al. 2008). In order to investigate whether a component of the Chefe Donsa eruption is preserved in the distal record, we turn to relatively nearby (200–300 km) depocenters in the west-central Afar region of Ethiopia (Hadar–Middle Awash and adjoining areas) where an abundant tephra archive exists; some of these tephra have previously been linked to source areas in the central sector of the MER and the northern Afar (Walter et al. 1987; Hart et al. 1992), as well as to distal tephra in Kenya, southern Ethiopia, and the Gulf of Aden (Sarna-Wojcicki et al. 1985; Brown et al. 1992; WoldeGabriel et al. 2005; Feakins et al. 2007). For example, the extensive investigations of the tephrochronology and stratigraphy of the Hadar and Busidima formations have generated a robust stratigraphic column against which the Chefe Donsa tephra may be evaluated (Walter and Aronson 1982; Hall et al. 1984; Campisano and Feibel 2008; Roman et al. 2008). On the basis of our Ar geochronology, the Chefe Donsa tephra producing event is temporally constrained between the well-characterized ~3.2-Ma Kada Hadar Tuff and ~2.94- to 2.96-Ma BKT-2 complex of the Hadar formation (Campisano and Feibel 2008).

Many Afar distal tephra units preserve compositionally complex glass compositions including multi-modal and continuous compositional spectrum varieties (Figs. 9, 10). As previously discussed, pumice and shards from Chefe Donsa display systematic chemical variation from trachyte through rhyolite. How does this systematic variation differ from the heterogeneities in the distal record? The Chefe Donsa $SiO_2$ distribution is rarely preserved in temporally equivalent Middle Awash tephra (Fig. 10) with the exception being true bimodal basalt/basaltic andesite–trachyte/rhyolite tephra where often additional shard compositions "intermediate" to these endmembers are preserved in small volume. Moreover, these bimodal/mixed tephra are known or inferred to have more proximal sources and even the high-$SiO_2$ endmembers are not widely distributed (Walter et al. 1987; WoldeGabriel et al. 2001; Kleinsasser et al. 2008; Hart and Woldegabriel 2010). The distal record can preserve very complex ranges in total Fe content even

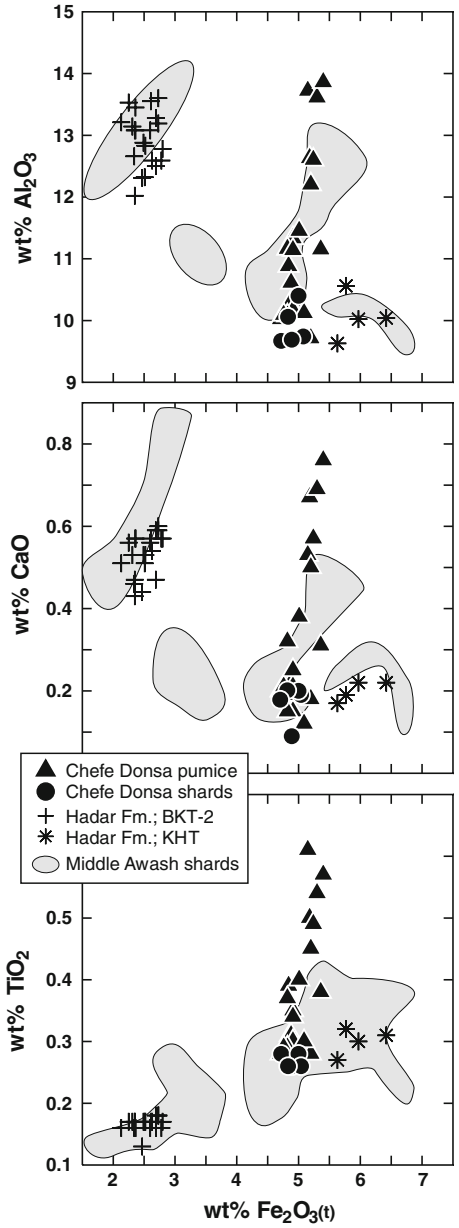


**Fig. 9** $Al_2O_3$, CaO, and $TiO_2$ versus $Fe_2O_3$(t) (total Fe as $Fe_2O_3$) for the Chefe Donsa pumice fragments and glass shard electron microprobe data (EMP). These are compared to sample-averaged (single and multiple populations) glass shard EMP data from the KHT and BKT-2 tephra units (Campisano and Feibel 2008; DiMaggio et al. 2008) and from Middle Awash tephra units with known or inferred ages of >2.7 to <3.4 Ma (Hart and WoldeGabriel 2010) and with a dominant chemical mode that overlaps in total Fe concentration with the Chefe Donsa materials

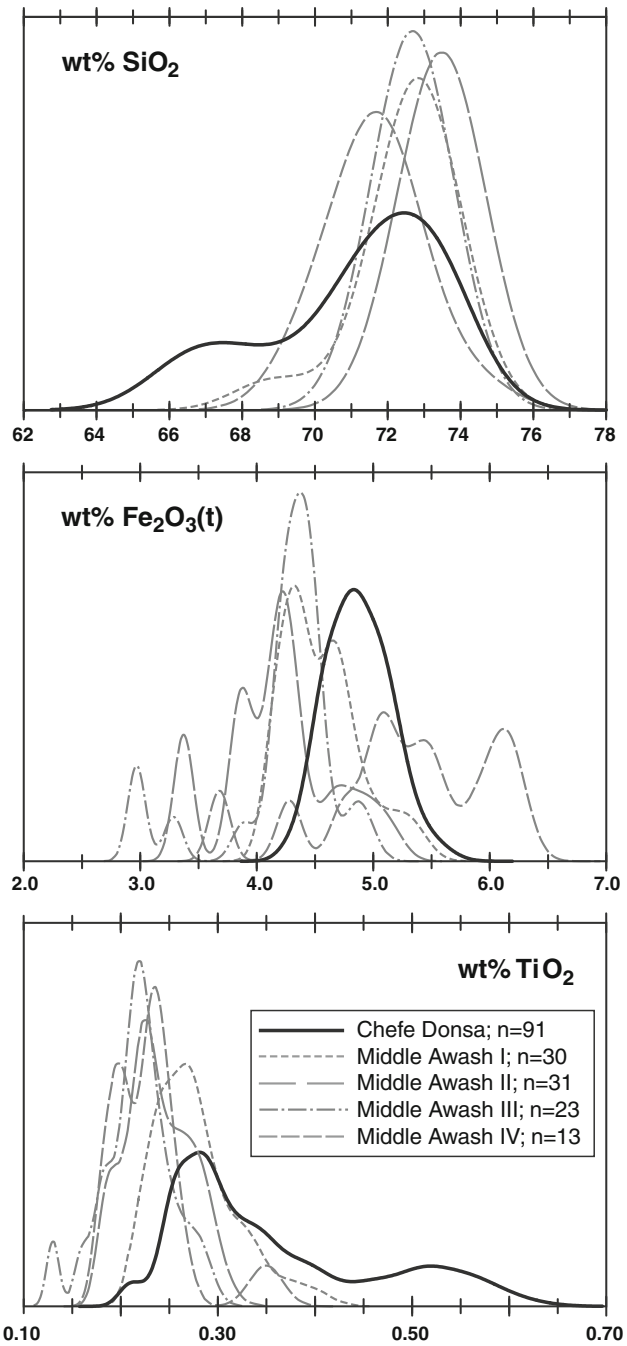


**Fig. 10** Cumulative Gaussian probability plots for individual glass shard/pumice spot EMP concentrations of $SiO_2$, $Fe_2O_3$(t), and $TiO_2$ for representative Middle Awash tephra (Hart and WoldeGabriel 2010) and for the Chefe Donsa proximal materials. These plots are interpreted in the same manner as, for example, are the Ar-Ar data in Fig. 6; tall narrow peaks indicate a high probability of encountering the corresponding *x*-axis value in a dataset

within a relatively narrow dominant $SiO_2$ range; this contrasts with the Chefe Donsa system which shows greater variability in Si than in Fe. Furthermore, the high Ti contents preserved in the less evolved Chefe Donsa samples are rarely observed in the distal tephra record except in mixed/mingled basalt-rhyolite tephra. The range of material represented by the Kada Hadar Tuff and BKT-2 tephra is therefore clearly distinct from the Chefe Donsa eruptive products. Moreover, no direct distal correlative of the Chefe Donsa eruption has been uncovered (Fig. 9). However, some overlap does exist between components of the Middle Awash record and glass shards at the low Al, Ca,

and Ti end of the Chefe Donsa compositional spectrum (Fig. 9). This is consistent with our observation that the glass shards analyzed from the Chefe Donsa deposit have a restricted composition and elevated values of $SiO_2$. The representation of the Chefe Donsa event in distal tephra deposits may therefore be as a tephra population with a restricted compositional range, making comparison between proximal and distal deposits on the basis of total compositional range unreliable.

## Conclusions

The evolution of a peralkaline magma may be effectively explained by the extensive fractional crystallization of a variably contaminated basaltic parental magma. Thermodynamic models show a close match between modeled and observed major element characteristics of the Chefe Donsa glasses; however, inconsistencies in CaO and $P_2O_5$ reflect the important role of flour-apatite in such systems. The influence of fluorine on peralkaline rocks is recognized; however, there are currently few experimental constraints as to the stability of F-bearing phases, impeding the development of effective thermodynamic models in such systems.

Our results are consistent with previous studies that have investigated the evolution of peralkaline magma in the region (e.g., Peccerillo et al. 2003); however, a significant barrier to the fractional crystallization model is the difficulty of segregating small degrees of Si-rich residual melts from the large crystalline masses. The limited variation in mode and chemical heterogeneity of the crystal cargo of the Chefe Donsa deposits highlights the necessity of a crystal mush model in explaining the evolution of this system. On the basis of these models (e.g., Bachmann and Bergantz 2004, 2008; Dufek and Bachmann 2010; Deering et al. 2011b), we suggest a two-step polybaric process for the formation of the Chefe Donsa deposits. Firstly, the differentiation of basaltic magma in the Ethiopian mid-upper crust results in the effective extraction of residual liquids broadly similar to the most primitive magmas at Chefe Donsa once the degree of crystallinity reaches a stage where a rigid framework is formed at ~50–60 % (Bachmann and Bergantz 2008). Although the composition of the melt extracted at this locking point is dependent on the initial basaltic parent, for initial basalts at 7–8 % MgO, the calculated composition of the residual liquid at the 50–60 % locking point is comparable to the most primitive Chefe Donsa pumice. The trachytic magma extracted during the first model step will ascend and continue crystallizing, forming a second crystal mush at shallower levels in the crust. Rhyolitic magmas equivalent to the most evolved Chefe Donsa pumice may be extracted from this mush when sufficient crystallization has occurred (~70 %), consistent with our MELTS modeling. Intrusion of fresh trachytic magma into the system may explain some of the range of compositions observed and provide a triggering mechanism for eruption. This model has significant implications for our understanding of silicic magmatism in the MER. In particular, the observed regional Daly Gap (Peccerillo et al. 2007) may result from the requirement for a rigid crystalline framework so as to allow for the extraction of magmas with more evolved compositions (Bachmann and Bergantz 2008; Dufek and Bachmann 2010). The eruptibility of these extracted magmas is dependent on vapor saturation, and further exploration of the role of F in such saturation and in influencing the crystallization assemblage is necessary.

The observation of a substantial range in the chemical composition of the proximal deposits from the Chefe Donsa center has implications for proximal–distal tephra correlations. Deposits from within the Hadar and Middle Awash depocenters that are temporally equivalent to the Chefe Donsa eruption often exhibit a range of compositions from within the same horizon that might imply a source with magmatic heterogeneity similar to Chefe Donsa. Despite the array of compositions represented within the Chefe Donsa deposits, we have shown that there is no clear correlation between the Chefe Donsa products and these other tephra deposits. In particular, the less evolved compositions at the lower end of the $SiO_2$ spectrum have substantially different $TiO_2$ contents, though some overlap with tephra from the regional depocenters is observed at higher values of $SiO_2$. Compositionally homogeneous tephra, akin to the limited compositional range noted for the Chefe Donsa shards, dominate the distal tephra record but compositionally heterogeneous tephra are an important component. These heterogeneous deposits when deemed primary likely reflect an eruptive episode from a single volcanic center that captured in its explosivity a more representative range of compositions present within the magmatic system just prior to eruption. The conditions and processes leading to differences between such systems and those like Chefe Donsa warrant additional investigation. If, as our results suggest, distal tephra shards potentially do not faithfully represent the array of glass compositions produced during a single magmatic event, then robust proximal–distal tephra correlation must include a careful analysis of a range of materials in the proximal deposit ranging from pumice to glass shards.

**Acknowledgments** Thoughtful comments by Olivier Bachmann and an anonymous reviewer helped improve the manuscript. We thank Timothy Grove for careful editorial handling and helpful suggestions.

## References


Annen C, Sparks RSJ (2002) Effects of repetitive emplacement of basaltic intrusions on thermal evolution and melt generation in the crust. Earth Planet Sci Lett 203(3–4):937–955

Annen C, Blundy JD, Sparks RSJ (2006) The genesis of intermediate and silicic magmas in deep crustal hot zones. J Petrol 47(3):505–539

Avanzinelli R, Bindi L, Menchetti S, Conticelli S (2004) Crystallisation and genesis of peralkaline magmas from Pantelleria Volcano, Italy: an integrated petrological and crystal-chemical study. Lithos 73(1–2):41–69

Ayalew D (2011) The relations between felsic and mafic volcanic rocks in continental flood basalts of Ethiopia: implication for the thermal weakening of the crust. In: Van Hinsbergen DJJ, Buiter SJH, Torsvik TH, Gaina C, Webb SJ (eds) The formation and evolution of Africa: a synopsis of 3.8 Ga of earth history. Geological Society, London, Special Publication, London, pp 253–264

Ayalew D, Ishiwatari A (2011) Comparison of rhyolites from continental rift, continental arc and oceanic island arc: implication for the mechanism of silicic magma generation. Island Arc 20:78–93

Bachmann O, Bergantz GW (2004) On the origin of crystal-poor rhyolite: extracted from batholithic crystal mushes. J Petrol 45(8):1565–1582

Bachmann O, Bergantz GW (2008) Rhyolites and their source mushes across tectonic settings. J Petrol 49(12):2277–2285

Barberi F, Ferrara G, Santacroce R, Treuil M, Varet J (1975) A transitional basalt-pantellerite sequence of fractional crystallization, the Boina Centre (Afar Rift, Ethiopia). J Petrol 16(1):22–56

Bilham R, Bendick R, Larson K, Mohr P, Braun J, Tesfaye S, Asfaw L (1999) Secular and tidal strain across the main Ethiopian rift. Geophys Res Lett 26(18):2789–2792

Bonini M, Corti G, Innocenti F, Manetti P, Mazzarini F, Abebe T, Pecskay Z, (2005) Evolution of the Main Ethiopian Rift in the frame of Afar and Kenya rifts propagation. Tectonics, 24(1): TC1007, doi: 10.1029/2004TC00168

Boynton WV (1984) Cosmochemistry of the rare earth elements: meteorite studies. In: Henderson P (ed) Rare earth element geochemistry. Elsevier, New York

Brown FH, Sarna-Wojcicki AM, Meyer CE, Haileab B (1992) Correlation of Pliocene and Pleistocene tephra layers between the Turkana Basin of East Africa and the Gulf of Aden. Quat Int 13–14:55–67

Buck WR (2004) Consequences of asthenospheric variability on continental rifting. In: Karner G, Taylor B, Driscoll NW, Kohlstedt DL (eds) Rheology and deformation of the lithosphere at continental margins. Columbia University Press, New York, pp 1–30

Campisano C, Feibel CS (2008) Tephrostratigraphy of the Hadar and Busidima Formations at Hadar, Afar Depression, Ethiopia. In: Quade J, Wynn JG (eds) The geology of early humans in the horn of Africa, special paper 446. The Geological Society of America, Boulder, Co, pp 135–162

Casey M, Ebinger C, Keir D, Gloaguen R, Mohamed F (2006) Strain accommodation in transitional rifts: extension by magma intrusion and faulting in Ethiopian rift magmatic segments. In: Yirgu G, Ebinger C, Maguire P (eds) The Afar Volcanic Province within the East African Rift System. Geological Society, London, pp 143–164

Deer WA, Howie RA, Zussman J (1996) An introduction to the rock-forming minerals, 2nd edn. Prentice Hall, New York

Deering CD, Bachmann O, Dufek J, Gravley DM (2011a) Rift-related transition from andesite to rhyolite volcanism in the Taupo Volcanic Zone (New Zealand) controlled by crystal–melt dynamics in mush zones with variable mineral assemblages. J Petrol 52(11):2243–2263

Deering CD, Bachmann O, Vogel TA (2011b) The Ammonia Tanks Tuff: erupting a melt-rich rhyolite cap and its remobilized crystal cumulate. Earth Planet Sci Lett 310(3–4):518–525

DiMaggio EN, Campisano CJ, Arrowsmith JR, Reed KE, Swisher CC, III, Lockwood CA (2008) Correlation and stratigraphy of the BKT-2 volcanic complex in west-central Afar, Ethiopia. In: Quade J, Wynn JG (eds) The geology of early humans in the horn of Africa, special paper 446. Geological Society of America, Boulder, CO, pp 163–177

Dufek J, Bachmann O (2010) Quantum magmatism: magmatic compositional gaps generated by melt-crystal dynamics. Geology 38(8):687–690

Ebinger CJ, Casey M (2001) Continental breakup in magmatic provinces: an Ethiopian example. Geology 29(6):527–530

Feakins SJ, Brown FH, deMenocal PB (2007) Plio-Pleistocene microtephra in DSDP site 231, Gulf of Aden. J Afr Earth Sc 48(5):341–352

Furman T, Kaleta KM, Bryce JG, Hanan BB (2006) Tertiary mafic lavas of Turkana, Kenya: constraints on East African plume structure and the occurrence of high-mu volcanism in Africa. J Petrol 47(6):1221–1244

Gasparon M, Innocenti F, Manetti P, Peccerillo A, Tsegaye A (1993) Genesis of the Pliocene to Recent bimodal mafic-felsic volcanism in the Debre Zeyit area, central Ethiopia; volcanological and geochemical constraints. J Afr Earth Sci 17(2):145–165

George R, Rogers N, Kelley S (1998) Earliest magmatism in Ethiopia: evidence for two mantle plumes in one flood basalt province. Geology 26(10):923–926

Ghiorso MS, Sack RO (1995) Chemical mass-transfer in magmatic processes. 4. A revised and internally consistent thermodynamic model for the interpolation and extrapolation of liquid-solid equilibria in magmatic systems at elevated-temperatures and pressures. Contrib Miner Petrol 119(2–3):197–212

Gualda GAR, Ghiorso MS, Lemons RV, Carley TL (2012) Rhyolite-MELTS: a modified calibration of MELTS optimized for silica-rich, fluid-bearing magmatic systems. J Petrol. doi:10.1093/petrology/egr080

Hall CM, Walter RC, Westgate JA, York D (1984) Geochronology, stratigraphy and geochemistry of Cindery Tuff in Pliocene hominid-bearing sediments of the Middle Awash, Ethiopia. Nature 308(5954):26–31

Hart WK, Woldegabriel G (2010) Tephra as Probes into magma system evolution and regional tectonomagmatic processes in the Ethiopian and Afar Rifts. INQUA/INTAV-J, 2010 Abstracts. Kirishima City, Japan

Hart WK, Walter RC, WoldeGabriel G (1992) Tephra sources and correlations in Ethiopia: application of elemental and neodymium isotope data. Quat Int 13–14:77–86

Heumann A, Davies GR (2002) U-Th disequilibrium and Rb-Sr age constraints on the magmatic evolution of Peralkaline Rhyolites from Kenya. J Petrol 43(3):557–577

Hofmann C, Courtillot V, Feraud G, Rouchett P, Yirgu G, Ketefo E, Pik R (1997) Timing of the Ethiopian flood basalt event and implications for plume birth and global change. Nature 389(6653):838–841

Kieffer B, Arndt N, Lapierre H, Bastien F, Bosch D, Pecher A, Yirgu G, Ayalew D, Weis D, Jerram DA, Keller F, Meugniot C (2004) Flood and shield basalts from Ethiopia: magmas from the African superswell. J Petrol 45(4):793–834

Kleinsasser LL, Quade J, McIntosh WC, Levin NE, Simpson SW, Semaw S (2008) Stratigraphy and geochronology of the late Miocene Adu-Asa Formation at Gona, Ethiopia. In: Quade J, Wynn JG (eds) The geology of early humans in the horn of

Africa. Geological Society of America Special Paper 446, Boulder, CO, pp 33–65
Lahitte P, Gillot P-Y, Courtillot V (2003) Silicic central volcanoes as precursors to rift propagation; the Afar case. Earth Planet Sci Lett 207(1–4):103–116
Le Maitre RW (2002) Igneous rocks: a classification and glossary of terms. Cambridge University Press, Cambridge
MacDonald R, Scaillet B (2006) The central Kenya peralkaline province: insights into the evolution of peralkaline salic magmas. Lithos 91(1–4):59–73
MacDonald R, Davies GR, Bliss CM, Leat PT, Bailey DK, Smith RL (1987) Geochemistry of High-silica Peralkaline Rhyolites, Naivasha, Kenya Rift Valley. J Petrol 28(6):979–1008
MacDonald R, Baginski B, Belkin HE, Dzierzanowski P, Jezak L (2008) REE partitioning between apatite and melt in a peralkaline volcanic suite, Kenya Rift Valley. Mineral Mag 72(6): 1147–1161
Marshall AS, MacDonald R, Rogers NW, Fitton JG, Tindle AG, Nejbert K, Hinton RW (2009) Fractionation of Peralkaline Silicic Magmas: the Greater Olkaria Volcanic Complex, Kenya Rift Valley. J Petrol 50(2):323–359
Mohr PA (1961) The geology, structure, and origin of the Bishoftu explosion craters. Bull Geophys Obs 2(2):65–101
Mohr PA (1967) Major volcano-tectonic lineament in the Ethiopian rift system. Nature 213(5077):664–665
Mohr P, Zanettin B (1988) The Ethiopian flood basalt province. In: MacDougall JD (ed) Continental flood basalts. Kluwer, Dordrecht, pp 63–110
Morton WH, Rex DC, Mitchell JG, Mohr P (1979) Riftward younging of volcanic units in the Addis Ababa region, Ethiopian Rift valley. Nature 280(5720):284–288
Murphy MD, Sparks RSJ, Barclay J, Carroll MR, Brewer TS (2000) Remobilization of Andesite Magma by Intrusion of Mafic Magma at the Soufriere Hills Volcano, Montserrat, West Indies. J Petrol 41(1):21–42
Nakamura M (1995) Continuous mixing of crystal mush and replenished magma in the ongoing Unzen eruption. Geology 23(9):807–810
Pallister JS, Hoblitt RP, Reyes AG (1992) A basalt trigger for the 1991 eruptions of Pinatubo volcano? Nature 356(6368):426–428
Pearce JA, Harris NBW, Tindle AG (1984) Trace element discrimination diagrams for the tectonic interpretation of granitic rocks. J Petrol 25(4):956–983
Peccerillo A, Barberio MR, Yirgu G, Ayalew D, Barbieri M, Wu TW (2003) Relationships between mafic and peralkaline silicic magmatism in continental rift settings: a petrological, geochemical and isotopic study of the Gedemsa volcano, central Ethiopian rift. J Petrol 44(11):2003–2032
Peccerillo A, Donati C, Santo AP, Orlando A, Yirgu G, Ayalew D (2007) Petrogenesis of silicic peralkaline rocks in the Ethiopian rift: geochemical evidence and volcanological implications. J Afr Earth Sci 48(2–3):161–173
Perkins ME, Nash BP (2002) Explosive silicic volcanism of the Yellowstone hotspot: the ash fall tuff record. Geol Soc Am Bull 114(3):367–381
Roman DC, Campisano C, Quade J, DiMaggio E, Arrowsmith JR (2008) Composite tephrostratigraphy of the Dikika, Gona, Hadar, and Ledi-Geraru project areas, northern Awash, Ethiopia. In: Quade J, Wynn JG (eds) The geology of early humans in the horn of Africa, Special Paper 446. Geological Society of America, Boulder, Co, pp 119–134
Rooney TO (2010) Geochemical evidence of lithospheric thinning in the southern Main Ethiopian Rift. Lithos 117(1–4):33–48
Rooney T, Furman T, Yirgu G, Ayalew D (2005) Structure of the Ethiopian lithosphere: Xenolith evidence in the Main Ethiopian Rift. Geochim Cosmochim Acta 69(15):3889–3910
Rooney T, Furman T, Bastow ID, Ayalew D, Gezahegn Y (2007) Lithospheric modification during crustal extension in the Main Ethiopian Rift. J Geophys Res B Solid Earth Planets 112: B10201, doi:10.1029/2006JB004916
Rooney T, Sinha AK, Deering CD, Briggs C (2010) A model for the origin of rhyolites from South Mountain, Pennsylvania: implications for rhyolites associated with large igneous provinces. Lithosphere 2(4):211–220
Rooney TO, Bastow ID, Keir D (2011) Insights into extensional processes during magma assisted rifting: evidence from aligned scoria cones and maars. J Volcanol Geoth Res 201(1–4): 83–96
Rooney TO, Hanan BB, Graham DW, Furman T, Blichert-Toft J, Schilling J-G (2012) Upper mantle pollution during afar plume–continental rift interaction. J Petrol 53:365–389
Ruprecht P, Bachmann O (2010) Pre-eruptive reheating during magma mixing at Quizapu volcano and the implications for the explosiveness of silicic arc volcanoes. Geology 38(10): 919–922
Sarna-Wojcicki AM, Meyer CE, Roth PH, Brown FH (1985) Ages of tuff beds at East African early hominid sites and sediments in the Gulf of Aden. Nature 313(6000):306–308
Scaillet B, MacDonald R (2001) Phase relations of peralkaline silicic magmas and petrogenetic implications. J Petrol 42(4):825–845
Scaillet B, MacDonald R (2003) Experimental constraints on the relationships between peralkaline rhyolites of the Kenya rift valley. J Petrol 44(10):1867–1894
Shane P, Nairn IA, Martin SB, Smith VC (2008) Compositional heterogeneity in tephra deposits resulting from the eruption of multiple magma bodies: Implications for tephrochronology. Quat Int 178(1):44–53
Sparks SRJ, Sigurdsson H, Wilson L (1977) Magma mixing: a mechanism for triggering acid explosive eruptions. Nature 267(5609):315–318
Trua T, Deniel C, Mazzuoli R (1999) Crustal control in the genesis of Plio-Quaternary bimodal magmatism of the Main Ethiopian Rift (MER); geochemical and isotopic (Sr, Nd, Pb) evidence. Chem Geol 155(3–4):201–231
USGS (2004) Shuttle Radar Topography Mission 1 arc second scene unfilled, unfinished 2.0. Global Land Cover Facility, University of Maryland., College Park, Maryland
van Wyk de Vries B, Merle O (1998) Extension induced by volcanic loading in regional strike-slip zones. Geology 26(11):983–986
Walter RC, Aronson JL (1982) Revisions of K/Ar ages for the Hadar hominid site, Ethiopia. Nature 296(5853):122–127
Walter RC, Hart WK, Westgate JA (1987) Petrogenesis of a basalt-rhyolite tephra from the west-central Afar, Ethiopia. Contrib Miner Petrol 95(4):462–480
WoldeGabriel G, Aronson JL, Walter RC (1990) Geology, geochronology, and rift basin development in the central sector of the Main Ethiopia Rift. Geol Soc Am Bull 102(4):439–458
Woldegabriel G, Heiken G, White T, Asfaw B, Hart WK, Renne PR (2000) Volcanism, tectonism, sedimentation, and the paleoanthropological record in the Ethiopian Rift System. In: McCoy FW, Heiken G (eds) Volcanic hazards and disasters in human antiquity. Geological Society of America Special Paper 345, Boulder, CO, pp 83–99
WoldeGabriel G, Haile-Selassie Y, Renne PR, Hart WK, Ambrose SH, Asfaw B, Heiken G, White T (2001) Geology and palaeontology of the Late Miocene Middle Awash valley, Afar rift, Ethiopia. Nature 412(6843):175–178
WoldeGabriel G, Hart WK, Katoh S, Beyene Y, Suwa G (2005) Correlation of Plio-Pleistocene Tephra in Ethiopian and Kenyan rift basins: temporal calibration of geological features and hominid fossil records. J Volcanol Geoth Res 147(1–2): 81–108

Wolfenden E, Ebinger C, Yirgu G, Deino A, Ayalew D (2004) Evolution of the northern Main Ethiopian rift: birth of a triple junction. Earth Planet Sci Lett 224(1–2):213–228

Yirgu G, Dereje A, Peccerillo A, Barberio MR, Donati C, Donato P (1999) Fluorine and chlorine distribution in the volcanic rocks from Gedemsa Volcano, Ethiopian Rift valley. Acta Vulcanol 11(1):169–176

Zanettin B, Justin Visentin E, Nicoletti M, Piccirillo EM, Carrelli A (1979) Correlations among Ethiopian volcanic formations with special references to the chronological and stratigraphical problems of the "Trap Series". Geodynamic evolution of the Afro-Arabian Rift System, 47: 231–252